Flow over periodic hills – Numerical and experimental study in a wide range of Reynolds numbers

M. Breuer [a,*], N. Peller [b], Ch. Rapp [b], M. Manhart [b]

[a] *Lehrstuhl für Strömungsmechanik, Universität Erlangen-Nürnberg, D-91058 Erlangen, Germany*
[b] *Fachgebiet Hydromechanik, Technische Universität München, D-80290 München, Germany*

ARTICLE INFO

ABSTRACT

The paper presents a detailed analysis of the flow over smoothly contoured constrictions in a plane channel. This configuration represents a generic case of a flow separating from a curved surface with well-defined flow conditions which makes it especially suited as benchmark case for computing separated flows. The hills constrict the channel by about one third of its height and are spaced at a distance of 9 hill heights. This setup follows the investigation of Fröhlich et al. [Fröhlich J, Mellen CP, Rodi W, Temmerman L, Leschziner MA. Highly resolved large-eddy simulation of separated flow in a channel with streamwise periodic constrictions. J Fluid Mech 2005;526:19–66] and complements it by numerical and experimental data over a wide range of Reynolds numbers. We present results predicted by direct numerical simulations (DNS) and highly resolved large-eddy simulations (LES) achieved by two completely independent codes. Furthermore, these numerical results are supported by new experimental data from PIV measurements. The configuration in the numerical study uses periodic boundary conditions in streamwise and spanwise direction. In the experimental setup periodicity is achieved by an array of 10 hills in streamwise direction and a large spanwise extent of the channel. The assumption of periodicity in the experiment is checked by the pressure drop between consecutive hill tops and PIV measurements. The focus of this study is twofold: (i) Numerical and experimental data are presented which can be referred to as reference data for this widely used standard test case. Physical peculiarities and new findings of the case under consideration are described and confirmed independently by different codes and experimental data. Mean velocity and pressure distributions, Reynolds stresses, anisotropy-invariant maps, and instantaneous quantities are shown. (ii) Extending previous studies the flow over periodic hills is investigated in the wide range of Reynolds numbers covering $100 \leqslant Re \leqslant 10{,}595$. Starting at very low Re the evolution and existence of physical phenomena such as a tiny recirculation region at the hill crest are documented. The limit to steady laminar flow as well as the transition to a fully turbulent flow stage are presented. For $700 \leqslant Re \leqslant 10{,}595$ turbulent statistics are analyzed in detail. Carefully, undertaken DNS and LES predictions as well as cross-checking between different numerical and experimental results build the framework for physical investigations on the flow behavior. New interesting features of the flow were found.

© 2008 Elsevier Ltd. All rights reserved.

1. Introduction

1.1. Case definition

The prediction of flow separation from curved surfaces and subsequent reattachment is complicated by several phenomena including irregular movement of the separation and reattachment lines in space and time, strong interactions with the outer flow, transition from a boundary layer type of flow to a separated shear layer with failure of the law-of-the wall and standard model assumptions for either attached flows or free shear layers. The

improvement of flow prediction by Reynolds-averaged Navier–Stokes (RANS) simulation or large-eddy simulation (LES) in such flows is dependent on reliable data of generic test cases including the main features of the respective flow phenomena. The flow over periodically arranged hills in a channel as proposed by Mellen et al. [33] has been used as benchmark test case since it represents well-defined boundary conditions, can be computed at affordable costs and nevertheless inherits all the features of a flow separating from a curved surface and reattaching on a flat plate. The geometry of the test case is shown in Fig. 1. The dimensions of the domain are $L_x = 9.0h$, $L_y = 3.036h$, and $L_z = 4.5h$, where h denotes the hill height.

In order to motivate why this case is especially useful for basic investigations of the performance of turbulence models – not only subgrid-scale (SGS) models but also statistical models in the RANS
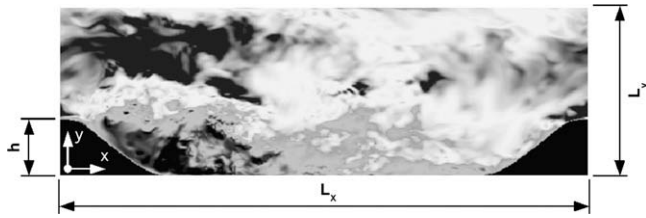

Fig. 1. Sketch of the flow geometry and snapshot of instantaneous streamwise velocity at $Re = 5600$.

context –, and other issues such as wall modeling, the history how this test case was established is briefly sketched.

Almeida et al. [1,2] experimentally investigated the flow behind two-dimensional model hills. Two different configurations were considered, i.e., the flow over a single hill and the flow over periodic hills. In 1995 these experiments were chosen as the basis of a test case at the ERCOFTAC/IAHR workshop held in Karlsruhe by Rodi et al. [42]. In order to select the least demanding configuration, the periodic arrangement without side walls was considered. However, the calculations carried out for this test case highlighted a number of serious problems and open questions, see [33]. This concerns the unknown influence of the side walls in the experiment not taken into account in the predictions. Since the aspect ratio in the experiment was small (almost square cross-section), it was expected that the spanwise confinement provoked spanwise variations. Furthermore, the predictions at the workshop [42] have cast doubt on the true periodicity of the experimental setup leading to the fact that simulations and experiment were not comparable. Another critical point is the high Reynolds number. Based on the hill height h and the mean centerline velocity the Reynolds number was $Re = 60,000$. Since the channel height in the experiment was large ($L_y = 6.071h$), the corresponding Reynolds number based on L_y is even about six times larger resulting in high computational costs for the configuration chosen. This problem even increases if the single hill case is considered for which suitable experimental data are available. The unknown effect of the side walls remains for this case. Therefore, a new configuration was defined by Mellen et al. [33], which leans on the experimental setup by Almeida et al. [1] but avoids the problems discussed above.

The re-definition of the test case also allows to meet a number of desiderata judged to be associated with a good test case for LES studies [33,48]. The flow has to contain the key generic phenomena of interest, whilst being amenable to a simulation at economically tolerable cost. The new geometry is sketched in Fig. 1. The shape of the hill is taken from the study of Almeida et al. [1]. An accurate geometric specification is available in form of a polynomial ansatz [2].

First, compared with Almeida et al.'s configuration the distance between two hill crests in streamwise direction was doubled. This increased distance allows the flow to reattach naturally between successive hills, providing a significant post-reattachment-recovery region on the flat plate between the two hills prior to the reacceleration over the next hill. From the numerical and modeling point of view this modification means that reattachment is now strongly influenced by wall modeling, SGS modeling, and grid arrangement issues. This aspect was not obvious in the original configuration since reattachment was dictated by the presence of the windward face of the consecutive hill.

Second, the original channel height was halved. This measure reduces the computational effort and allows a higher aspect ratio L_z/L_y.

Third, the side walls existing in the original experimental setup of Almeida et al. [1] are removed and instead periodicity in the spanwise direction is assumed. Based on additional investigations by Mellen et al. [33] a spanwise extension of the computational domain of $L_z = 4.5h$ was recommended for LES or hybrid LES–RANS predictions.

Fourth, the Reynolds number was reduced and set to $Re = 10,595$ where $Re = U_B h/v$ is based on the hill height h, the bulk velocity U_B taken at the crest of the first hill and the kinematic viscosity v of the fluid. Furthermore, the flow is assumed to be periodic in the streamwise direction which represents a simple way out of the dilemma to specify appropriate inflow boundary conditions for LES or DNS. For that purpose the increase of the distance between two consecutive hills described above is beneficial too, since it enhances the streamwise decorrelation. Thus, a well-defined flow state independent of inflow conditions is achieved.

As a consequence the resulting geometrically simple test case offers a number of important features challenging from the point of view of turbulence modeling and simulation. The pressure-induced separation takes place from a continuous curved surface and reattachment is observed at the flat plate (see Fig. 1). Hence, these flow features are sensitive to numerical and modeling aspects. Therefore, this configuration was already a test case at various workshops, e.g., the *ERCOFTAC/IAHR/COST Workshops on Refined Turbulence Modeling* in 2001 [22] and 2002 [29], respectively. Consequently, a variety of predicted results using RANS as well as LES are available which can only be partially cited in the succeeding section.

1.2. Previous studies

The periodic hill flow test case has been studied so far pursuing two main objectives, either the *modeling and simulation* issue or the *physical* issue. Regarding the first, it is used as a benchmark case to investigate the ability of RANS and LES to resolve separation from a curved geometry. Furthermore, the flow is also an interesting case to study the *physical* mechanisms of separation on curved surfaces in more detail.

1.2.1. Modeling and simulation issue

Besides the workshops mentioned above [22,29] a few more studies on the *modeling and simulation* issue should be provided first emphasizing on LES. Temmerman and Leschziner [47] investigated the periodic hill flow at $Re = 10,595$ using LES. The emphasis was on the effectiveness of different combinations of subgrid-scale models and wall functions on relatively coarse grids. The accuracy was judged by reference to a wall-resolved simulation (lower wall only) on a grid with about 4.6 million nodes. It was demonstrated [47] that even gross-flow parameters, such as the length of the separation bubble, are very sensitive to modeling approximations (SGS and wall models) and the grid quality. A similar investigation was carried out by Mellen et al. [33] assessing the impact of different SGS models and the effect of grid refinement. In the succeeding study by Temmerman et al. [48] the previous efforts of both groups were combined and a comparative investigation was carried out applying three grids, six SGS models and eight practices of approximating the near-wall region. Again the coarse-grid simulations were judged by wall-resolved simulations using the fine grid mentioned above and two independent codes. The simulations on coarse grids highlighted the outstanding importance of an adequate streamwise resolution of the flow in the vicinity of the separation line. The main reason is the high sensitivity of the reattachment position to that of the separation. Furthermore, the near-wall treatment was found to be more influential on the quality of the results obtained on coarse grids than the subgrid-scale modeling.

In the meantime several studies used this test case to evaluate the performance not only for coarse-grid LES predictions but also for different kinds of hybrid LES–RANS approaches including detached-eddy simulations (DES), see, e.g. [10,12,14,43]. The latter for example was a collaborative effort involving five different flow solvers used by five different groups in order to cover a broad range of numerical methods and implementations. All simulations were

conducted on the same grid with approximately one million cells and compared to a highly resolved LES by Breuer [9]. Overall the DES predictions and also LES predictions on the same grid were found to be in good agreement with the reference data. Further coarsening of the grid did not alter the performance of DES substantially unless the LES–RANS interface moves outside the boundary layer on the crest of the hill. In that situation a massive deterioration of the results was detected.

To evaluate the performance of wall models for LES of attached flows the turbulent plane channel flow [25,34] is the standard test case. That is due to its geometrical simplicity including two homogeneous directions which allow the application of periodic boundary conditions avoiding inflow and outflow boundary conditions completely. For the development and investigation of wall models for separated flows, the channel flow with periodic constrictions has nearly reached an equivalent status and meaning. Similar to the plane channel the computational setup of the hill flow is simple owing to the possibility to apply periodic boundary conditions twice. However, for the hill case the flow separates from a curved surface and a large back-flow region emerges. Further downstream the flow reattaches and is accelerated at the windward side of the hill. Therefore, the separation and reattachment process can be studied in detail and wall models developed for attached and separated flows can be evaluated based on this flow.

As mentioned above, Temmerman et al. [48] investigated the predictive accuracy of different wall models based on this case. It was clearly shown that the predictions provided by classical wall models developed for attached flows are not satisfactory if the wall-nearest computational point is located outside the viscous sublayer. This renders the case as a sensitive platform to develop and improve wall models. For example, Manhart et al. [32] used this flow to evaluate a modified law of the wall for the viscous sublayer which accounts for the effect of both, the wall shear stress and the pressure gradient in the streamwise direction which plays an important role for separated flows. They analyzed the performance of this new formulation based on DNS data of the hill flow at $Re = 5600$. In similar investigations Breuer et al. [11,13] developed a new wall modeling strategy for separated flows. It allows to derive enhanced wall models which also take the streamwise pressure gradient into account. Moreover, the concept of artificial viscosity used for that purpose makes an accurate description of the physics of the flow in the wall-nearest region possible. Statistical evaluations of highly resolved LES data for the hill flow case using non-linear stochastic estimation were carried out in order to determine the important physical dependence involved in the new wall model, namely the ratio of the thickness of the viscous sublayer to the height of the wall-nearest cell. The results show that the enhanced wall model yields reliable predictions for separated flows. The agreement with the reference data was found to be much better than the results obtained by no-slip boundary conditions or classical wall models such as those by Schumann [44] and Werner and Wengle [49].

1.2.2. Physical issue

Concerning the *physical* issue a comprehensive investigation for the periodic hill flow at $Re = 10,595$ was carried out by Fröhlich et al. [18] based on LES predictions with about 4.6 million nodes and two independent codes. By the arguments given in Section 1.1 and especially the distinct post-reattachment-recovery region it is justified why the chosen configuration stands out from the crowd of investigations on flows over wavy-terrain geometries. A detailed analysis was carried out including the evaluation of the budgets for all Reynolds stress components, anisotropy measures, and spectra. The emphasis was on elucidating the turbulence mechanisms associated with separation, recirculation and acceleration. The statistical data were supported by investigations on the structural

features of the flow. Based on that interesting observations such as the very high level of spanwise velocity fluctuations in the post-reattachment zone on the windward hill side were explained. This phenomenon revealed to be a result of the 'splatting' of large-scale eddies originating from the shear layer and convected downstream towards the windward slope. That explains why RANS simulations even when applying second-moment closures can not capture the flow field accurately. As stated by the authors [18], the identification of other structures by means of structure-identification methods turned out to be difficult, mainly because of the high Reynolds number.

In [12] a preliminary study was carried out in which the Reynolds number effect was investigated for the first time. Interesting flow features such as the variation of the reattachment length were found. Furthermore, the existence of a tiny recirculation at the foot of the windward face of the hill reported in [18] was confirmed for $Re = 10,595$. That and other findings motivated to study the flow under varying Reynolds numbers more deeply.

1.3. Goals and outline of the present study

The objective of the present investigation is concerned with the *physical* issue of the periodic hill flow. Compared to the comprehensive study by Fröhlich et al. [18] it differs in a certain number of aspects. The first issue concerns the fundamentals of the investigations which besides two independent numerical simulation techniques also relies on experimental measurements (PIV) which were especially carried out for this work recently. The second important point is the extension to a wide range of Reynolds numbers including the one studied before, for which compared to [18] a refined simulation including the resolution of the upper wall region was performed. The extension to a broad range of Reynolds numbers allows one on the one hand to take also direct numerical simulations into account using grids with up to about a quarter of a billion grid points. On the other hand the influence of the Reynolds number on the statistical data as well as on the dynamical flow structures could be analyzed in detail. Since the key features of massively separated flows are assumed to be only weakly dependent on Re, structure-identification methods could be applied to the low-Re cases involved.

The remainder of the paper is organized as follows: In Section 2 the experimental setup is described. The computational methodologies and the numerical parameters pertaining to the simulations reported later are given in Section 3. That includes a thorough analysis of the resolution issue for both grid types applied. Section 4 delivers cross-comparisons between the different numerical results and the measured data. The influence of the Reynolds numbers on statistical as well as structural features of the flow field will be highlighted in Section 5. Conclusions are finally presented in Section 6.

2. Experimental setup

A water channel has been set up to investigate the flow experimentally (see Fig. 2). Water was chosen as its density is 800 times higher than that of air and its kinematic viscosity is 13 times lower. At the same model scale and Reynolds number the pressure in water is 4.5 times higher than in air and therefore easier to determine. The corresponding ratio for the characteristic times is 13. This issue contributes to higher accuracy especially in instantaneous flows [15]. The water was filtered, decalcified and chlorinated to avoid disturbances from lime stone and biofilm on the boundaries of the channel.

A well with a maximum discharge of 70 l/s pumps the water from a reservoir through a pipe with a diffuser into an intake
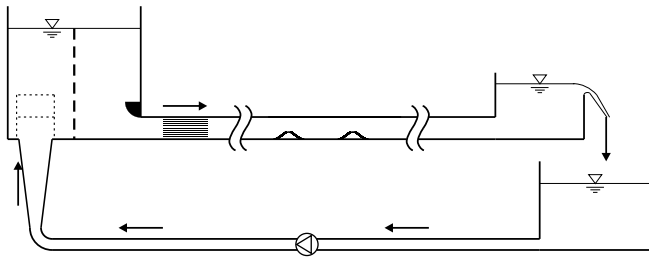
Fig. 2. Experimental setup for the flow over periodic hills.

reservoir that damps fluctuations. Several fixtures such as sieves, air intake filters and barriers abate the structures evolving from the entering jet. The rectangular channel which is $3.036h$ high and $18h$ wide is directly attached to the intake reservoir that is $18h$ wide as well. The dimensions of the model relate to the hill height h that was chosen to be 50 mm. The wider extend in the spanwise direction in comparison to the computational domain was chosen to accomplish homogeneity in the center part of the channel [40]. The first part of the channel that is $10h$ in length is followed by round flow straighteners that are approximately $0.44h$ in diameter and $10h$ long. A distance of $20h$ lies between the flow straighteners and the foot of the first hill. In total 10 hills were chosen to achieve periodicity in the streamwise direction [40], whereas the measurement section is between hill seven and eight. A rectangular section of $34h$ lies between the foot of hill 10 and the outlet reservoir. The water levels in the intake and outlet reservoir determine the pressure gradient and with it the Reynolds number.

The material mainly used is polyvinylchloride. Plexiglas and glass were chosen for the cover and the walls of the channel at the measurement section. The hills were cast from polyurethane in monolithic blocks. The achieved degree of accuracy of the setup is $\leqslant 0.01h$.

To check the periodicity in the streamwise direction 19 holes were drilled into the top cover of the channel at local positions $x/h = 1.3$ and $x/h = 6.3$ (see Fig. 3). They are located one hill height off the center plane in order not to disturb the PIV measurements that were carried out in the center. For control of the homogeneity in the spanwise direction the pressure was recorded at 14 locations at local positions $z/h = 1.2$ and $z/h = 7.8$ at hill eight.

2.1. Pressure measurements

Two pressure cells with an effective range of 1000 Pa and a specific error of 0.1% were chosen to acquire the pressure drop and the spanwise pressure distribution. The pressure was recorded relatively to the one on hill crest eight. It was acquired at a sample rate of 1000 Hz until the change in variance was less than 5×10^{-5}. Instantaneous data could not be evaluated, nevertheless, the mean values contributed to prove the comparability of the experiment to the numerical simulations in terms of periodicity and homogeneity [40]. At $Re = 5600$ the pressure drops between consecutive hill

tops can be seen as constant from hill four on. The spanwise pressure distribution on the leeward and windward side of the hill is constant in the range of accuracy of the pressure cells as well.

2.2. Velocity measurements

The velocity measurements were conducted with a two-dimensional PIV system. A 190 mJ NdYAG laser emitting 532 nm pulses was used to generate a light sheet that was 0.7 mm wide. The images were recorded with a 4 MPx CCD camera. They were streamed through a RAID system so that 10,000 double frames could be recorded at a frame rate of 7.25 f/s. The duration of the experiment corresponds to 335 flow-through times for $Re = 5600$ and 634 flow-through times for $Re = 10,595$, where the flow-through time is based on the distance between two consecutive hills and the bulk velocity U_B. Laser light reflections at the walls were avoided by adjusting the camera position in the particular optical axis. Therefore, six camera positions were necessary recording partially overlapping frames with a length/height of 2048 px, corresponding to 289 mm or 5.79 hill heights (see Fig. 3). The size of the interrogation areas is 32×32 pixels. They are overlapping by half of their side length. The spatial resolution corresponds to $\Delta_s = 2.279$ mm or 0.046 hill heights. Table 1 shows ratios of the side length of the interrogation areas Δ_s and the smallest scales in the DNS. The Kolmogorov scale $\eta_{\min}$ was taken from the DNS using $\mathcal{MGLET}$ (see case 8 in Table 3) at $Re = 5600$ and scaled by $Re^{3/4}$ for $Re = 10,595$. Since the smallest Kolmogorov length is locally varying, an averaged value denoted η_{mean} provides a more reasonable estimation on the spatial resolution and thus this ratio is added in Table 1.

2.2.1. Seeding particles

The purified water was seeded with hollow glass spheres. The major advantage of these particles is their dispersion behavior in water. They do not cluster and bright scattering leads to high-contrast images. The diameters of the spheres range from 8 µm to 12 µm, whereas their density varies from 0.1 g/cm³ to 1.5 g/cm³. The Stokes number of the particles, defined as

$$St = \frac{t_p}{t_k} \tag{1}$$

with the Kolmogorov time scale

$$t_k = \sqrt{\frac{\nu}{\epsilon}} \tag{2}$$

Table 1
Spatial resolution Δ_s of the PIV measurements with respect to the Kolmogorov scale η at three different streamwise locations

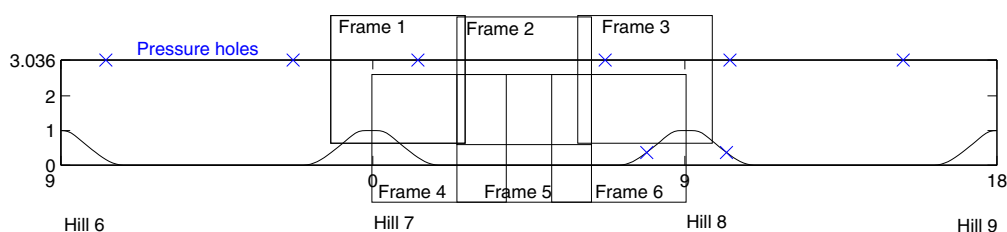| Re	Ratio	$x/h = 0.5$	$x/h = 1.0$	$x/h = 6.0$
5600	$\Delta_s/\eta_{\min}$	29.4	26.8	23.4
5600	$\Delta_s/\eta_{\text{mean}}$	17.2	17.5	16.0
10,595	$\Delta_s/\eta_{\min}$	47.5	23.3	37.7
10,595	$\Delta_s/\eta_{\text{mean}}$	27.8	28.3	25.8

Fig. 3. Measurement section between hill seven and eight.

Table 2
Variation of the Reynolds number in the experiment

Nominal Re	Re_{min}	Re_{max}
5600	5184	5291
10,595	10,979	11,144

and the particle time scale,

$$t_p = \frac{\rho_p}{\rho_f} \frac{d_p^2}{18\nu},$$

(3)

was calculated to check their behavior in the flow. The maximum Stokes number as a result of ϵ_{max}, the maximum dissipation in the flow field from the DNS using $\mathcal{MGLET}$ (see case 8 in Table 3) at $Re = 5600$, the greatest particle diameter d_p and the highest ratio of the particle's and fluid's density ρ_p/ρ_f is $St = 1.32 \times 10^{-2} \ll 1$. Hence, it can be assumed that the particles follow the flow within a sufficiently short time scale.

2.2.2. PIV algorithm

The minimum intensity image was subtracted from the individual images before the pixel intensity was doubled. The wide intensity distribution leads to high correlation peaks. For saving computational time cross-correlations have been conducted in Fourier space, using a so-called 'Recursive Nyquist Grid'. The velocity vectors were considered as valid if the magnitude of the streamwise component was within $[-0.75U_B; 1.7U_B]$ and the magnitude of the vertical component was within $[-0.75U_B; 0.75U_B]$. Afterwards the vectors were median-filtered, while a deviation of $0.4U_B$ from 3×3 surrounding vectors was tolerated. Skipped vectors were interpolated by means of 5×5 surrounding vectors. These vectors determine the initial shift of the second frame interrogation areas for the second processing run. After the final step about 1% of the vectors were interpolated.

The post-processing was conducted for data using first correlation peak vectors only and for data including also the interpolated vectors. A comparison of the two differently obtained results showed no deviations.

2.2.3. Conduction of the experiments

The experimental conditions were controlled through simultaneous temperature and discharge measurements (by a magneto inductive device, MID) at all times. Slight temperature variations ($\leqslant 0.4$ K) during the individual experimental runs led to changes in viscosity by less than 1.0%. The discharge was adjusted by a slide valve that can only be handled with a certain accuracy. With these boundary conditions, the Reynolds numbers achieved in the six individual experimental runs for each Reynolds number varied slightly as shown in Table 2.

The velocity fields of the six different frames were merged into joint profiles through integrations of the velocity profiles in overlapping parts of the six frames. These factors were counterchecked with the ratios of mean discharges recorded by the MID. The normalization of the velocities and the Reynolds stresses was done with respect to U_B that was acquired from the integration of the velocity profile at hill crest seven.

3. Numerical setup: methods and modeling approaches

3.1. Governing equations

For the DNS predictions of the present study we solve the three-dimensional, time-dependent Navier–Stokes equations for an incompressible fluid which reads in its dimensionless form:

$$\frac{\partial u_i}{\partial x_i} = 0,$$

(4)

$$\frac{\partial u_i}{\partial t} + \frac{\partial (u_i u_j)}{\partial x_j} = -\frac{\partial p}{\partial x_i} + \frac{1}{Re} \frac{\partial^2 u_i}{\partial x_j^2}.$$

(5)

Here, u_i, p and Re are the Cartesian velocity components, the pressure and the Reynolds number, respectively. In the LES predictions only the large energy-carrying eddies are computed directly whereas the influence of the small eddies has to be modeled by a subgrid-scale model. Consequently, the governing equations (4) and (5) have to be filtered in space leading to the so-called filtered Navier–Stokes equations which are similar to the original set of equations but contain the additional subgrid-scale stress tensor [8,39]. Its task is to mimic the influence of the non-resolved small-scale structures on the resolved large eddies.

3.2. Numerical methodologies

The numerical part of the present study relies on two completely independent codes based on either curvilinear body-fitted grids with a colocated variable arrangement or Cartesian non-uniform grids using a staggered configuration. The objective is to present highly reliable results obtained by carefully cross-checking between the outcome of both numerical schemes and additional experimental data. Afterwards the investigations concentrate on the physical aspects of the flow considered.

In the following, both codes are described briefly. For a more detailed description we refer to [5–8] for the code $\mathcal{LESOCC}$ and [30,31,35] for the code $\mathcal{MGLET}$. No attempt is made to explain all advantages and drawbacks of each method which would go beyond the scope of the present paper.

3.2.1. Finite-volume code $\mathcal{LESOCC}$

$\mathcal{LESOCC}$ solves the (filtered) Navier–Stokes equations based on a three-dimensional finite-volume method for arbitrary non-orthogonal and non-staggered block-structured grids (see, e.g., Fig. 4). The spatial discretization of all fluxes is based on central differences of second-order accuracy. Time advancement is performed by a predictor–corrector scheme. A low-storage multi-stage Runge–Kutta method (three substeps, second-order accuracy) is applied for integrating the momentum equations in the predictor step. Within the corrector step the Poisson equation for the pressure correction is solved implicitly by the incomplete LU decomposition method of Stone [46]. Explicit time marching works well for DNS and LES with small time steps which are necessary to resolve turbulence motion in time. In order to ensure the coupling of pressure and velocity fields on non-staggered grids, the momentum interpolation technique of Rhie and Chow [41] is used. For modeling the non-resolvable subgrid scales, two different models are implemented, namely the well-known Smagorinsky model [45] with Van Driest damping near solid walls and the dynamic approach with a Smagorinsky base model proposed by Germano et al. [19] and modified by Lilly [26]. In order to stabilize the dynamic model, averaging of the numerator and the denominator in the relation for the determination of the Smagorinsky value [19,26] was carried out in the spanwise homogeneous direction and also in time using a recursive digital low-pass filter [5,8]. The code and the implemented SGS models were validated on a variety of different test cases. For more information on this issue, please refer to [5–8].

$\mathcal{LESOCC}$ is highly vectorized and additionally parallelized by domain decomposition (see Fig. 4) with explicit message-passing based on MPI allowing efficient computations especially on vector-parallel machines and SMP clusters. The present simulations were carried out on the SMP-system Hitachi SR8000-F1, applying 8 nodes (= 64 processors). Related to the usage of a single Hitachi
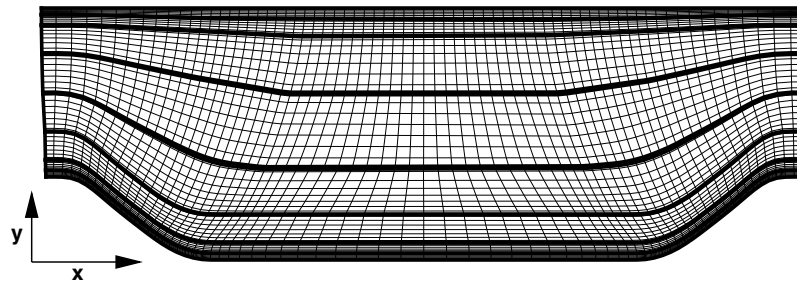
Fig. 4. Cross-section (x–y) of the curvilinear grid; every fourth grid line is shown; thick lines depict block boundaries.
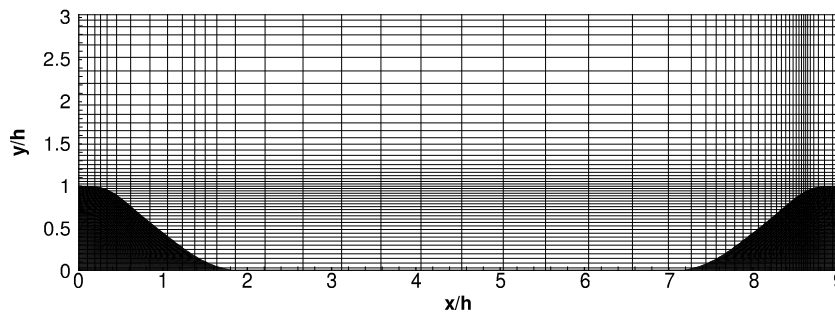

Fig. 5. Cross-section (x–y) of the Cartesian grid; every 15th grid line is shown.

node, the computing time per time step and control volume (CV) is about 2×10^{-6} s.

3.2.2. Finite-volume code $\mathcal{M}$GLET

$\mathcal{M}$GLET is based on a finite-volume formulation for non-uniform Cartesian grids with a staggered arrangement of the spatially filtered variables (see, e.g., Fig. 5). The spatial discretization of the convective and diffusive fluxes is based on second-order central differences. The momentum equations are advanced in time by a fractional time stepping using either an explicit second-order central leapfrog scheme (case 5[1]) or a third-order Runge–Kutta scheme (cases 3 and 8). For the solution of the Poisson equation for the pressure the 'strongly implicit procedure' (SIP) by Stone [46] is implemented. For the representation of the hill geometry in the Cartesian grid an immersed boundary technique is used. All Cartesian cells lying inside the body are excluded from the computation. The excluded cells are determined by the intersection of the hill geometry with the Cartesian cells. The geometry of the hills is represented by a triangle mesh. The immersed boundary technique provides a smooth representation of the body surface in the Cartesian mesh by using third-order least squares interpolation for the interface cells [35]. This method prevents instabilities which are present in high-order Lagrange interpolation schemes. The code is used for DNS and LES simulations. It has been shown by several authors that second-order accuracy can be sufficient for DNS of flows provided the grid resolution is sufficient [16,17,30].

$\mathcal{M}$GLET is highly vectorized and parallelized by domain decomposition using MPI. The simulations were performed on the Hitachi SR8000-F1, whereupon the DNS at $Re = 2800$ used 24 nodes and the DNS at $Re = 5600$ used 32 nodes. Related to the usage of a single Hitachi node, the computing time per time step and CV is about 9.6×10^{-7} s for the DNS at $Re = 5600$. For more information on the code, please refer to [31].

Hence, both codes are relying on the finite-volume method and are second-order accurate in space and time. The intrinsic difference is the type of grids used and related to that the representation of curved or oblique boundaries of the integration domain.

3.3. Boundary conditions and simulation parameters

Since the grid resolution in the vicinity of the wall is sufficient to resolve the viscous sublayer (see Section 3.4), the no-slip and impermeability boundary condition is used at the wall in both codes. The flow is assumed to be periodic in the streamwise direction and thus periodic boundary conditions are applied. Similar to the turbulent plane channel flow case the non-periodic behavior of the pressure distribution can be accounted for by adding the mean pressure gradient as a source term to the momentum equation in streamwise direction. Two alternatives exist. Either the pressure gradient is fixed which might lead to an unintentional mass flux in the configuration or the mass flux is kept constant which requires to adjust the mean pressure gradient in time. Since a fixed Reynolds number can only be guaranteed by a fixed mass flux, the second option is chosen using the method proposed by Benocci and Pinelli [4].

Furthermore, the flow is assumed to be homogeneous in spanwise direction and periodic boundary conditions are applied, too. For that purpose the use of an adequate domain size in the spanwise direction is of major importance in order to obtain reliable and physically reasonable results. To assure this criterion the two-point correlations in the spanwise direction have to vanish in the half-width of the domain size chosen. Based on the investigations by Mellen et al. [33] a spanwise extension of the computational domain of $L_z = 4.5h$ is used in all computations presented. This extension of the domain was also used in the investigation by Fröhlich et al. [18]. It represents a well-balanced compromise between spanwise extension and spanwise resolution.

Table 3 summarizes the most important parameters of the simulations available. N_{tot} denotes the total number of grid points used; the corresponding number of control volumes is slightly lower. Although a direct comparison of the number of grid points

---

[1] Reason: Runge–Kutta scheme not available at that time.

Table 3
Parameters of the simulations performed

Case	Re	Simulation	$N_{tot}/10^6$	N_{span}	$\Delta t/10^{-3}$	T_{avg}	Code
1	700	DNS	13.1	200	0.5	1581	$\mathcal{LESOCC}$
2	1400	DNS	13.1	200	1.1	1249	$\mathcal{LESOCC}$
3	1400	DNS	20.0	132	1.5	540	$\mathcal{MGLET}$
4	2800	DNS	13.1	200	2.0	1249	$\mathcal{LESOCC}$
5	2800	DNS	48.0	304	1.0	562	$\mathcal{MGLET}$
6	5600	DNS	13.1	200	2.0	1214	$\mathcal{LESOCC}$
7	5600	LES	13.1	200	2.0	1303	$\mathcal{LESOCC}$
8	5600	DNS	231.0	404	1.0	343	$\mathcal{MGLET}$
9	10,595	LES	13.1	200	1.8	1277	$\mathcal{LESOCC}$

used by $\mathcal{LESOCC}$ and $\mathcal{MGLET}$ in one x–y plane is not reasonable, at least the number of points equidistantly distributed in the spanwise direction, N_{span}, can be compared.

The dimensionless time-step size Δt is also tabulated in Table 3, where the time is normalized by the ratio of the hill height h and the bulk velocity U_B taken at the crest of the hill. To reduce statistical errors due to insufficient sampling to a reasonable minimum, the flow field was averaged in spanwise direction and in time over a long period of ΔT_{avg} which is also given in Table 3. Partially, ΔT_{avg} covers a time interval of about 140 flow-through times.

3.4. Resolution issues

In this section the choice of grids used in the present study will be motivated. It is divided into two subsections for the different numerical methods applied. Nevertheless, similar criteria are used to determine the appropriate grid design for both numerical schemes. Satisfying these criteria leads to different restrictions for both methods which are pointed out in the following. We start with the curvilinear grid design for the wall-resolved LES prediction at the highest Reynolds number chosen, i.e., $Re = 10,595$.
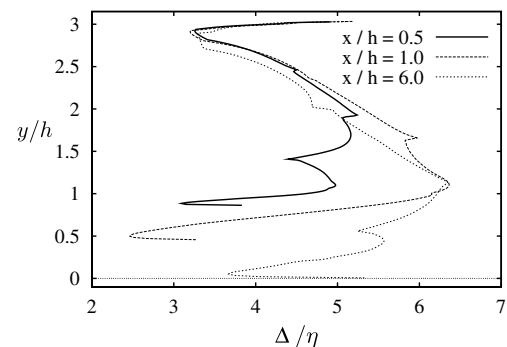
3.4.1. Curvilinear grids

For the simulation at $Re = 10,595$ $\mathcal{LESOCC}$ applies a curvilinear block-structured grid consisting of $N_{tot} = 13.1$ million grid points corresponding to a total of about 12.4 million control volumes. The grid points are clustered in the vicinity of the lower wall, the upper wall, and the region where the free shear layer appears. Besides classical quality criteria such as orthogonality and smoothness, two main issues motivated the distribution of the grid points in space. These are the resolution of the near-wall region and of the inner domain.

To evaluate the first concern, the most important quality criterion is the distribution of non-dimensional y^+ values defined by $y^+ = \Delta y_{cc} u_\tau / \nu$ where Δy_{cc} denotes the distance of the cell center from the wall and $u_\tau = \sqrt{\tau_w/\rho}$ describes the shear stress velocity. Note that due to the cell-centered variable arrangement Δy_{cc} is half of the corresponding cell height Δy. Fig. 6 depicts the y^+ distribution along the lower wall at all Reynolds numbers considered. At $Re = 10,595$ the values are below 0.45 with a mean value of about 0.2 except at the windward side of the hill. Here, the largest values of the wall shear stress are observed and the y^+ value reaches its maximum of about 1.2. Hence, the lower wall is well resolved. Regarding the wall-normal resolution the grid satisfies the requirements of a wall-resolved LES prediction. Compared to [18] who employed in their highly resolved simulations a curvilinear grid with about 4.6 million CVs ($196 \times 128 \times 186$) especially the number of grid points in the wall-normal direction was increased to 220 in the present investigation. Furthermore, the simulations resolve not only the lower wall (the hills) in more detail but also resolve the upper wall by a DNS-like representation ($y^+ \leqslant 0.95$ at $Re = 10,595$). Thus in contrast to [18] the application of wall func-
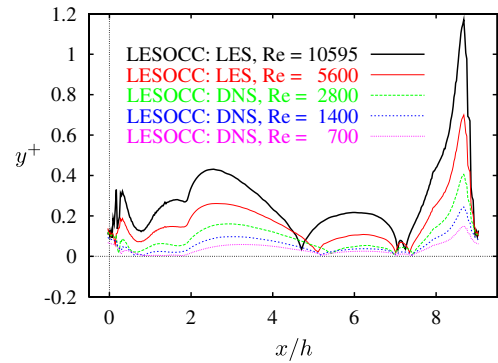
Fig. 6. Distribution of y^+ along the lower wall at different Re using $\mathcal{LESOCC}$.

tions is avoided. That allows to establish the influence of the resolution of the upper wall on the results. To prove the enhanced resolution, some numbers are provided. For instance, the cell sizes at the hill crest, which is a key region for the periodic hill flow are in the current case $\Delta x_{crest}/h = 0.026$ and $\Delta y_{crest}/h = 2.0 \times 10^{-3}$ whereas the corresponding values in [18] are $\Delta x_{crest}/h = 0.032$ and $\Delta y_{crest}/h = 3.3 \times 10^{-3}$, respectively. Owing to the increased resolution in streamwise and spanwise direction the cell sizes expressed in wall units are below $\Delta x^+ = 20$ and $\Delta z^+ = 9$ and thus lower than in [18] and substantially lower than the recommendations for wall-resolved LES given by Piomelli and Chasnov [38]. That also holds at the windward slope of the hill where the largest shear stresses are found.

To evaluate the second concern, the resolution of the inner region, it is reasonable to estimate the size of the smallest scales given by the Kolmogorov length $\eta = (\nu^3/\epsilon)^{1/4}$. In order to determine this quantity within the wall-resolved LES prediction, the dissipation tensor ϵ_{ij} was predicted and averaged in time and in spanwise direction. It has to be mentioned that this procedure represents only a rough estimate of ϵ_{ij} since on the one hand the diminutive SGS contribution is not included and on the other hand the present grid might slightly underestimate the dissipation tensor. Based on the dissipation rate $\epsilon = 1/2\epsilon_{ii}$ and the kinematic viscosity ν of the fluid, η can be determined and compared to the filter width $\Delta = (\Delta x \times \Delta y \times \Delta z)^{1/3}$ applied. In Fig. 7 profiles of Δ/η are shown at three different locations, $x/h = 0.5$, 1.0 and 6.0, respectively. With respect to the estimation given by Pope [39] that the maximum dissipation takes place at a length scale of about 24η, these structures are resolved by at least 4–5 grid points at $x/h = 0.5$. At $x/h = 1.0$ and 6.0 the maximum of Δ/η is about 6.3 and thus at least about four times smaller than the decisive scales found by Pope [39]. Consequently, the grid allows to resolve a

Fig. 7. Profiles of Δ/η at three different vertical positions: $x/h = 0.5$, 1.0, and 6.0; curvilinear grid used by $\mathcal{LESOCC}$ for the wall-resolved LES prediction at $Re = 10,595$.

substantial part of the dissipation. Overall the values Δ/η are smaller than in [18]. Especially, in the vicinity of the upper wall the situation is strongly improved.

As explained above the generation of the grid for $\mathcal{LES}OCC$ was designed for the wall-resolved LES predictions at $Re = 10,595$. Regarding the lower Reynolds numbers considered, the grid was not modified when Re was reduced. The reason is twofold. On the one hand a grid which is sufficiently fine for a certain Reynolds number should also be adequate for a lower Re. That is visible for example in Fig. 6 which depicts the distributions of y^+ along the lower wall for all Re. The shear stress increases with decreasing Reynolds numbers, but for fixed U_B and h the viscosity also increases with decreasing Re. As a result the average and maximum y^+ values are strongly reduced. Consequently, with decreasing Re the resolution becomes better and better. Thus by applying the same grid for the comparison of two Re, the effect of the grid is completely excluded from the consideration. On the other hand the intention was to perform DNS predictions for the lowest Reynolds numbers considered, i.e., at $Re = 700, 1400$, and 2800. Consequently, the grid should be sufficiently fine for a DNS at $Re = 2800$. That is exactly the Reynolds number in the classical plane channel flow predictions [25,34] who applied a grid of about 2 million points. In the present case a six times finer grid is applied which accounts for the more complex flow field and the lower accuracy of the numerical method. Besides the criteria discussed in detail above, a further evidence of the adequacy of the grid for DNS at $Re \leqslant 2800$ is provided by two simulations carried out at $Re = 5600$ (see Table 3). One simulation was done as a wall-resolved LES using the dynamic SGS model (case 7) and the other was carried out without a subgrid-scale model (case 6). As will be discussed below, only marginal deviations were found between both cases. That is a clear hint that for the further reduced Reynolds numbers $Re \leqslant 2800$ the grid used delivers results which can be regarded as DNS.

In accordance with [18] the simulation at $Re = 10,595$ (case 9) was performed with the dynamic Smagorinsky model. Owing to the increased resolution the ratio of v_t/v found in the present prediction is smaller than in the previous study. Moreover, by applying two different SGS models which delivered strongly differing eddy-viscosity values, Fröhlich et al. [18] have shown that the influence of this deviation on the LES prediction is low if a very fine grid is used as in the present case. That confirms that the present simulation is not materially inferior to a DNS near the walls.

Besides, for some additional simulations at very low Reynolds number between 100 and 700 to be discussed in Section 5.5, a coarser grid with $164 \times 100 \times 64$ CVs was used.

3.4.2. Cartesian grids

Also for the Cartesian grid used by $\mathcal{M}GLET$ the Kolmogorov scale in the domain and the resolution at the wall based on the wall shear stress are the most important criteria. Additional criteria have been established for the immersed boundary method. A first evaluation of these criteria has been obtained by preliminary simulations with relatively coarse grids. The finally computed values then confirmed these resolution estimations [36].

For the DNS at $Re = 2800$ (case 5) the grid is refined by geometric stretching in y-direction close to the hill surface where strong gradients must be resolved. The stretching factors are kept below 3%. Due to the Cartesian grid the refinement in y-direction is not exactly wall normal at all positions of the geometry. The grid spacings in streamwise and spanwise direction are equidistant. The simulation yields 48 million grid points.

For the DNS at $Re = 5600$ (case 8) the mesh is additionally stretched in x-direction. It is refined more closely according to the average wall shear stress at the bottom wall. Fig. 8 shows a plot of the grid spacings in x- and y-direction as well as the wall-normal distance of the pressure cell center d^+ from the geometry. d^+ is a measure to check the variation in the distance of grid points, which exists in immersed boundaries. If the variation is bounded as observed in Fig. 8, the body surface is well resolved even when it is not grid aligned. Determining the grid spacing and stretching is an iterative procedure in order to minimize the amount of grid cells used, because for Cartesian grids small grid spacing leads to a large number of grid points also in regions where it is not needed. Therefore, it is important to reduce the number of grid points by stretching at positions with low wall shear stress and condensing the number of grid points at locations with high wall shear stress. The wall-normal distance d^+ should remain at (or below) $d^+ \approx 1$ over the complete domain (see Fig. 8). The stretching factor is also required to stay below 3% for the DNS.

The resulting grid spacing with respect to the Kolmogorov length scale Δ/η can be seen in Fig. 9 for the same three representative positions as discussed in the section about the curvilinear grid. The inner domain is well resolved and the grid spacing does not exceed 2.2 times the Kolmogorov length scale. This also resolves scales well beyond the maximum dissipation rate at 24η as stated by Pope [39]. As it is known that the smallest scales exist in the turbulent boundary layer, Fig. 9 shows that the grid stretching compensates for the decrease in Kolmogorov length scale. The ratio Δ/η remains small at the wall.

Stretching and condensing the grid in x- and y-direction also effects the aspect ratio of the cells. For the DNS prediction (case 8) the aspect ratio $\Delta x/\Delta y$ is depicted in Fig. 8. It varies over
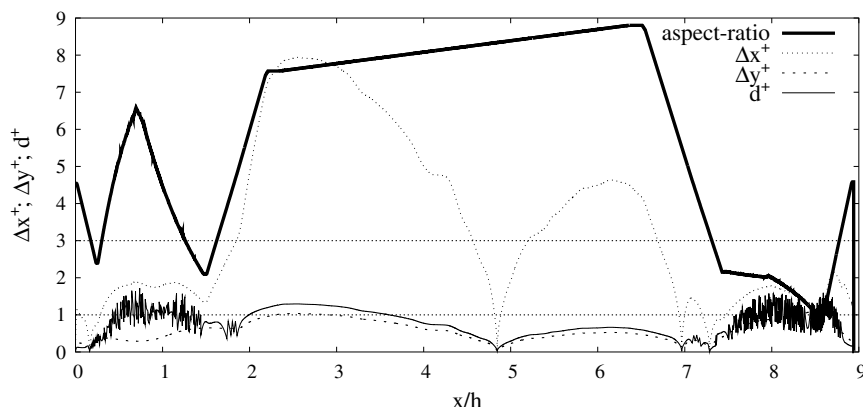

Fig. 8. Properties of the grid used by $\mathcal{M}GLET$ for the DNS prediction at $Re = 5600$ (case 8). Shown are grid spacings in wall units for x- and y-direction. Aspect ratio $\Delta x/\Delta y$ and resulting distance d^+ in wall units are plotted.
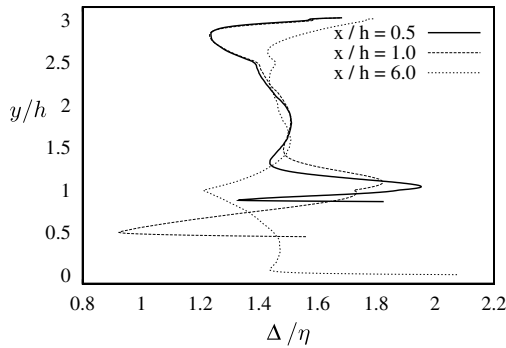
Fig. 9. Profiles of Δ/η at three different vertical positions: $x/h = 0.5$, 1.0, and 6.0; Cartesian grid used by $\mathcal{M}GLET$ for the DNS prediction at $Re = 5600$ (case 8).

the domain length since the grid stretching in x- and y-direction is adapted to the regions of high wall shear stress.

This leads to an optimization procedure for the grid generation in Cartesian meshes with immersed boundaries. It consists of four criteria: (i) Keeping the absolute wall-normal distance at $d^+ \approx 1$, (ii) the stretching ratio at $\approx 3\%$, (iii) the aspect ratio below 9 and (iv) assuring small grid spacings in relation to the Kolmogorov length scale in the entire domain. Applying these criteria the DNS grid (case 8) yields 231 million grid points.

With the same optimization procedure the grid for the DNS at $Re = 1400$ (case 3) is designed. Considering the lower Reynolds number, less points are needed and the grid consists of 20 million grid points.

4. Cross-comparison of results

4.1. Numerical results at Re = 2800 and 5600

Before investigating the flow physics and working out the influence of the Reynolds number, a cross-comparison of the results achieved by the different methods is carried out. For that purpose two different Reynolds numbers will be considered. According to Table 3 two DNS predictions are available at $Re = 2800$. Case 4 was performed by $\mathcal{L}ESOCC$ using a curvilinear grid and case 5 is based on $\mathcal{M}GLET$ using a Cartesian grid with about 3.5 times more grid points. At $Re = 5600$ case 7 is taken into account which denotes a wall-resolved LES prediction on the curvilinear grid. On the same grid a simulation without any SGS model was carried out (see case 6 in Table 3). However, the deviations found between cases 6 and 7 are marginal. This outcome is consistent with the very low eddy viscosities observed in case 7 which demonstrate that the resolution is nearly sufficient for a DNS ($v_t/v < 0.5$ for nearly all grid points of the instantaneous flow field). Nevertheless, as a matter of confidence the wall-resolved LES prediction (case 7) is preferred for the cross-comparison. These results are compared

with case 8 providing numerical data on an extremely fine Cartesian grid (231 million grid points) which based on the outcome of Section 3.4 is beyond all doubt a well-resolved DNS. The cross-comparison was also conducted for $Re = 1400$. However, since no new findings compared to the outcome presented in the following sections resulted, for the sake of brevity this Reynolds number is omitted here.

4.1.1. Global view of the flow

A global view of the flow from the DNS at $Re = 5600$ is given by the streamlines plot of the averaged flow field in Fig. 10 (case 8, Table 3). The flow separates at the hill crest at $x/h \approx 0.18$ and forms a large separation bubble reaching to $x/h \approx 5.1$. The separation in this case is not only due to an adverse pressure gradient but also the result of the strong streamwise curvature of the lower wall.

Fig. 11(a) displays the distribution of the averaged wall shear stress τ_w on the lower wall for the cases mentioned above. At both Re the flow separates shortly behind the hill crest where with increasing Re the separation point is moving upstream as visible in Fig. 22. Reattachment takes place about 5.1–5.4 hill heights behind the crest where both codes predict a somewhat larger recirculation length at $Re = 2800$ compared with $Re = 5600$. Fig. 22 displaying the separation and reattachment length predicted by both codes clearly shows that the results are in excellent agreement regarding these integral quantities (see Section 5 for a detailed discussion of this issue).

Downstream of the reattachment region a small recirculation zone just before the second hill at $x/h \approx 7$ is found which forms in all simulations. Along the ascent the wall shear stress strongly increases and reaches its maximum shortly before the hill crest. As will be discussed in detail in Section 5, the peak values of τ_w strongly increases with decreasing Re. The overall comparison of τ_w in Fig. 11(a) shows on the one hand an excellent agreement between the results of both codes at $Re = 2800$ and 5600 except at the windward side of the hill. On the other hand the dependence of the wall shear stress on the Reynolds number can be clearly appreciated (see Section 5 for a detailed discussion).

The deviations between the predictions of $\mathcal{L}ESOCC$ and $\mathcal{M}GLET$ observed at the windward side are attributed to the immersed boundary technique used on the Cartesian grid. It is much more elaborated to reconstruct the wall shear stress for the immersed boundary technique than for the curvilinear approach. The body surface is not aligned with the Cartesian grid and velocity values or derivatives of velocities, respectively, must be transformed into the wall-aligned coordinate system. As mentioned in Section 3.4.2 there is a variation in the wall-normal distance when considering the position of the velocity and pressure variables. In addition to that the variables are staggered and must be interpolated onto the same position. These two drawbacks, (i) the variation and (ii) the staggered arrangement make it difficult to reconstruct the wall shear stress along oblique walls accurately. However, the deviation in the wall shear stress does not seem to be an indication for
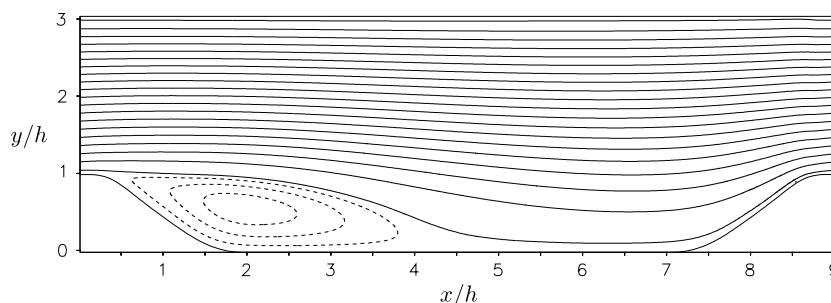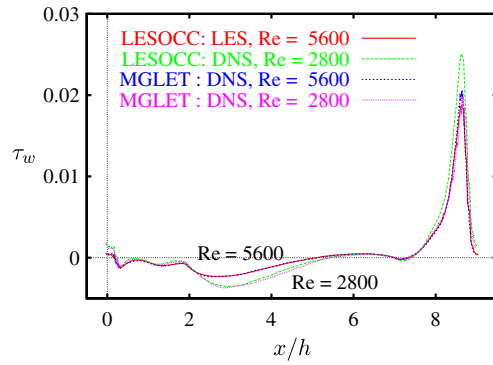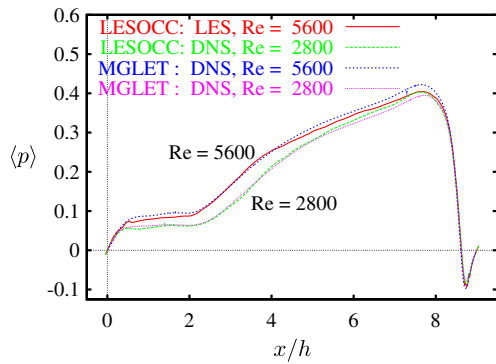

Fig. 10. Streamlines of the time-averaged flow field predicted by DNS at $Re = 5600$ (case 8, Table 3).

(a) Wall shear stress

(b) Pressure distribution

Fig. 11. Comparison of predictions by $\mathcal{L}$ESOCC and $\mathcal{M}$GLET for the averaged wall shear stress τ_w and the averaged pressure distribution $\langle p \rangle$ at the lower wall for two different Reynolds numbers, i.e., $Re = 2800$ (cases 4 and 5) and 5600 (cases 7 and 8 in Table 3, respectively).

deficiencies in the overall flow field. Velocity profiles (see Section 4.1.2) at the position of maximum wall shear stress agree well for the Cartesian and the curvilinear grid.

Finally, Fig. 11(b) depicts the distribution of the averaged pressure along the lower wall. As expected a plateau is observed in the recirculation region which is longer at $Re = 2800$ than at $Re = 5600$ and thus consistent with the reattachment lengths found at both Re. Similar to τ_w some small deviations between the simulations by $\mathcal{L}$ESOCC and $\mathcal{M}$GLET are found which are again mainly attributed to difference in the discretization especially along the inclined slopes. However, since in incompressible flows the pressure distribution shows an elliptic behavior, this discrepancy is already visible in front of the windward side of the hill. A second reason causing some minor deviations with respect to the maximum of the averaged pressure occurring at about $x/h = 7.8$ for $Re = 5600$ is given by the fact that one simulation represents an LES (case 7) whereas the other is a DNS (case 8). If the SGS model is switched off as it was done in case 6, the agreement between the results of $\mathcal{L}$ESOCC and $\mathcal{M}$GLET (not shown here) is slightly better with respect to the maximum, thus a small influence of the SGS model is present in case 7.

4.1.2. Averaged velocity and Reynolds stress profiles

Fig. 12 shows exemplarily the distribution of the averaged streamwise velocity $\langle U \rangle/U_B$ at four different vertical positions in the flow field, i.e., $x/h = 0.5, 2, 4$, and 6. The first position is located shortly after the separation line and crosses the strong shear layer; the second profile is at the beginning of the flat floor and hence within the main recirculation region. The third one is located near the end of the recirculation bubble and finally the last is positioned behind the main separation region in the reattached flow. At both Re the agreement observed between the results obtained by the different numerical methods is excellent. Only marginal deviations
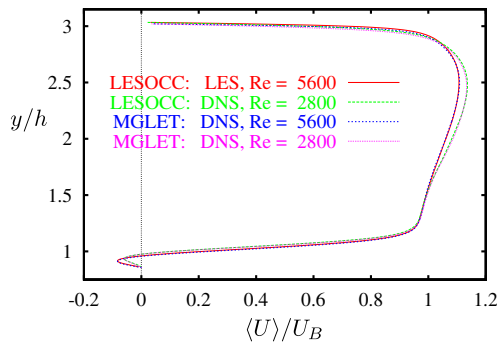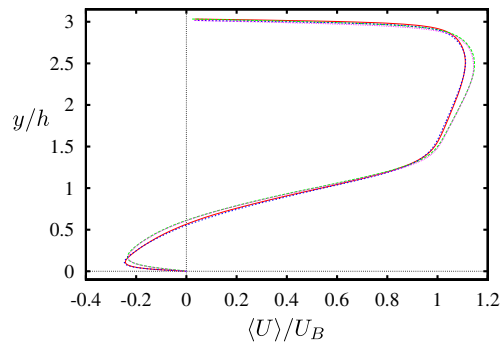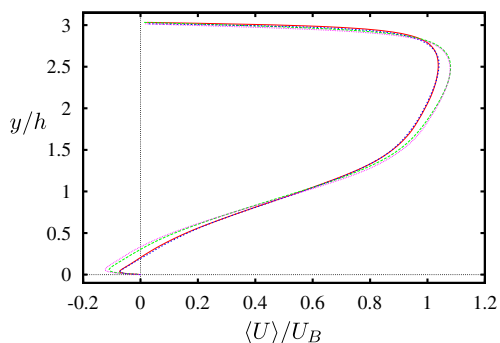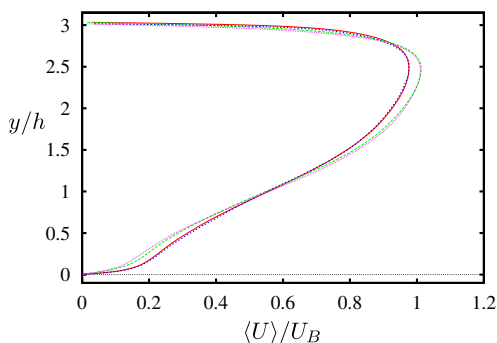

(a) $x/h = 0.5$

(b) $x/h = 2$.

(c) $x/h = 4$.

(d) $x/h = 6$.

Fig. 12. Comparison of predictions by $\mathcal{L}$ESOCC and $\mathcal{M}$GLET based on the streamwise velocity profiles $\langle U \rangle/U_B$ at four different locations ($x/h = 0.5, 2, 4$, and 6) and two different Reynolds numbers, i.e., $Re = 2800$ (cases 4 and 5) and 5600 (cases 7 and 8 in Table 3, respectively).
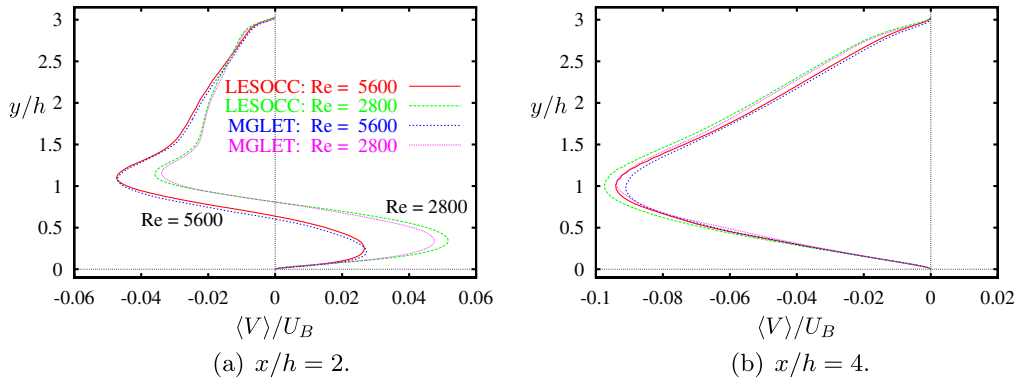
Fig. 13. Comparison of predictions by $\mathcal{LESOCC}$ and $\mathcal{MGLET}$ based on the normal velocity profiles $\langle V\rangle/U_B$ at two different locations ($x/h = 2$ and 4) and two different Reynolds numbers, i.e., $Re = 2800$ (cases 4 and 5) and 5600 (cases 7 and 8 in Table 3, respectively).

are found. For example, $\mathcal{MGLET}$ predicts slightly larger back-flow velocities at $x/h = 4$ for $Re = 2800$ compared with the data of $\mathcal{LESOCC}$. This marginal deviation is still visible further downstream at $x/h = 6$ close to the lower wall. Besides that the profiles resulting from the two independent simulation techniques lie on top of each other at both Re.

Fig. 13 depicts the distribution of the averaged normal velocity $\langle V\rangle/U_B$ at two locations in the middle and near the end of the recirculation bubble, i.e., $x/h = 2$, and 4. To evaluate this quantity it has to be taken into account that the normal velocity $\langle V\rangle$ is about a factor of 20 ($x/h = 2$) or 10 ($x/h = 4$) smaller than the streamwise velocity $\langle U\rangle$, respectively. At both Reynolds number the agreement

between the predictions by $\mathcal{MGLET}$ and $\mathcal{LESOCC}$ is extremely good. Small deviations are visible near the extrema, especially at $x/h = 4$. However, expressed in terms of the bulk velocity U_B the maximum deviation of $\langle V\rangle/U_B$ is about 0.4% and hence acceptable.

Furthermore, Figs. 14–16 display the resolved Reynolds stresses $\langle u'u'\rangle/U_B^2$, $\langle v'v'\rangle/U_B^2$, and $\langle u'v'\rangle/U_B^2$ at the same locations as in Fig. 13. The two main observations are as follows: First, a clear trend is obvious concerning the variation of the Reynolds stresses with varying Reynolds numbers. This issue will be addressed in detail in Section 5. Second, a reasonable agreement is found between the predictions based on the two different codes at both Re. Similar to the normal velocity component $\langle V\rangle$ small deviations are visible
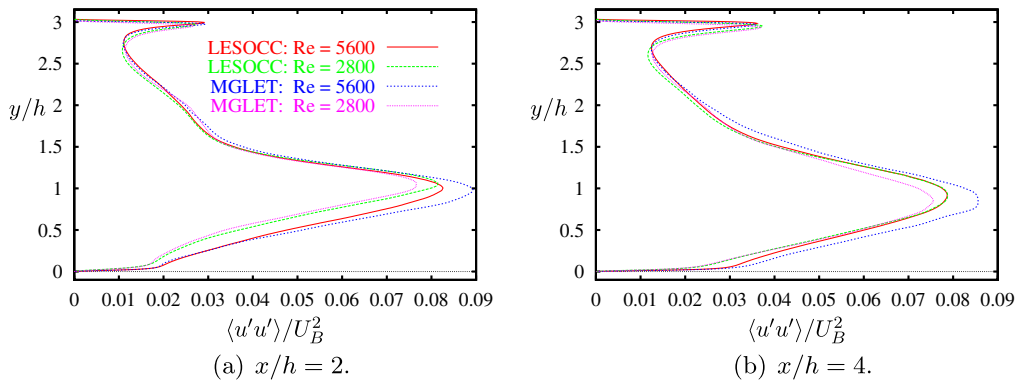

Fig. 14. Comparison of predictions by $\mathcal{LESOCC}$ and $\mathcal{MGLET}$ based on the normal Reynolds stress $\langle u'u'\rangle/U_B^2$ at two different locations ($x/h = 2$ and 4) and two different Reynolds numbers, i.e., $Re = 2800$ (cases 4 and 5) and 5600 (cases 7 and 8 in Table 3, respectively).
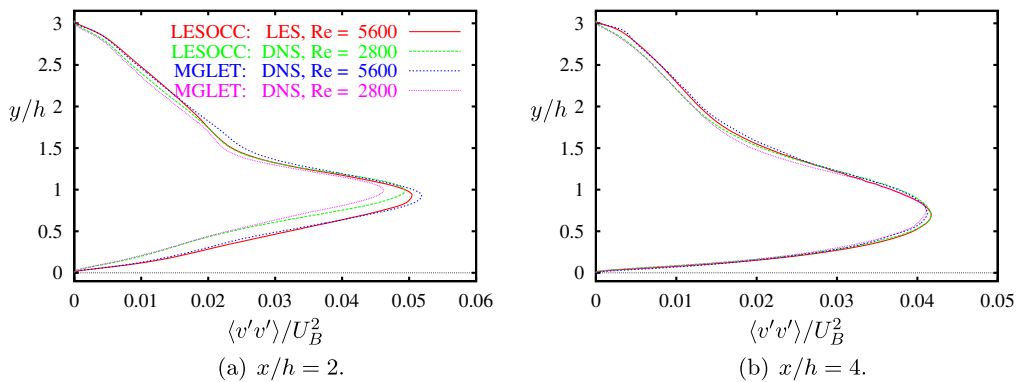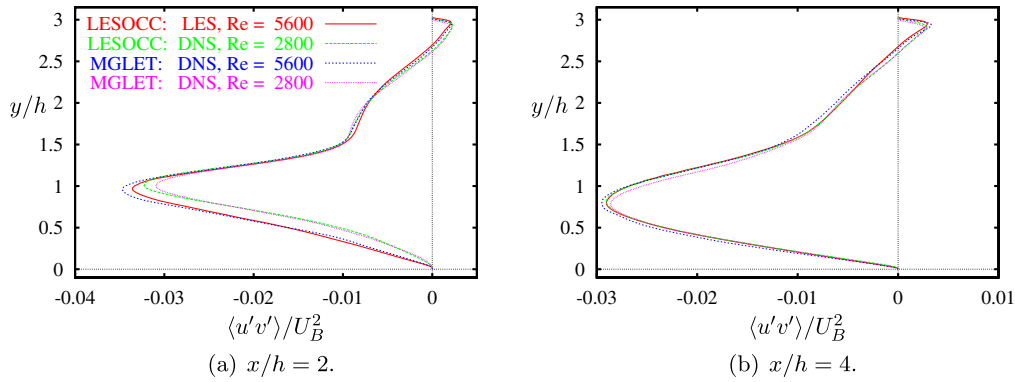

Fig. 15. Comparison of predictions by $\mathcal{LESOCC}$ and $\mathcal{MGLET}$ based on the normal Reynolds stress $\langle v'v'\rangle/U_B^2$ at two different locations ($x/h = 2$ and 4) and two different Reynolds numbers, i.e., $Re = 2800$ (cases 4 and 5) and 5600 (cases 7 and 8 in Table 3, respectively).

Fig. 16. Comparison of predictions by $\mathcal{L}ESOCC$ and $\mathcal{M}GLET$ based on the shear stress $\langle u'v'\rangle/U_B^2$ at two different locations ($x/h = 2$ and 4) and two different Reynolds numbers, i.e., $Re = 2800$ (cases 4 and 5) and 5600 (cases 7 and 8 in Table 3, respectively).

near the extrema occurring in the free shear layer. Except in this narrow region the normal stresses and the shear stress belonging to a certain Re agree satisfactorily. The extremely well-resolved prediction by $\mathcal{M}GLET$ at $Re = 5600$ (case 8 in Table 3) shows the largest peak values for $\langle u'u'\rangle/U_B^2$. The extrema of the normal stress $\langle v'v'\rangle/U_B^2$ as well as the shear stress $\langle u'v'\rangle/U_B^2$ in the shear layer ($x/h = 2$) are also slightly larger than the results predicted by $\mathcal{L}ESOCC$ (case 7). The deviations found at this Reynolds number can be explained by the fact that the last is an LES prediction whereas $\mathcal{M}GLET$ provides DNS data. The modeled stress contributions, although known to be small, are not taken into account in the LES data at $Re = 5600$ in Figs. 14–16.

4.2. Numerical results at Re = 10,595

Furthermore, the wall-resolved LES prediction by $\mathcal{L}ESOCC$ (case 9) is compared with literature data [18]. For this comparison

one should bear in mind that both simulations are based on similar numerical techniques (second-order accurate in space and time using curvilinear grids), but the main issues from Section 3.4 about the resolution should be recapitulated. The present grid consists of about three times more grid points than that used in [18] whereby the increased number of points is especially applied in the wall-normal direction to resolve also the upper wall and thus to avoid wall functions.

Fig. 17 depicts a comparison at three different locations ($x/h = 0.5$, 2, and 6) showing averaged velocity profiles for $\langle U\rangle/U_B$ and $\langle V\rangle/U_B$ as well as turbulent quantities such as the resolved turbulent kinetic energy $\langle k\rangle/U_B^2 = 0.5(\langle u'u'\rangle + \langle v'v'\rangle + \langle w'w'\rangle)/U_B^2$ and the shear stress $\langle u'v'\rangle/U_B^2$. For the streamwise velocity component $\langle U\rangle/U_B$ it is obvious that a very good agreement can be observed in the lower part of the computational domain close to the lower wall. Solely in the vicinity of the upper wall deviations are visible which can be assigned to the application of wall functions in [18].
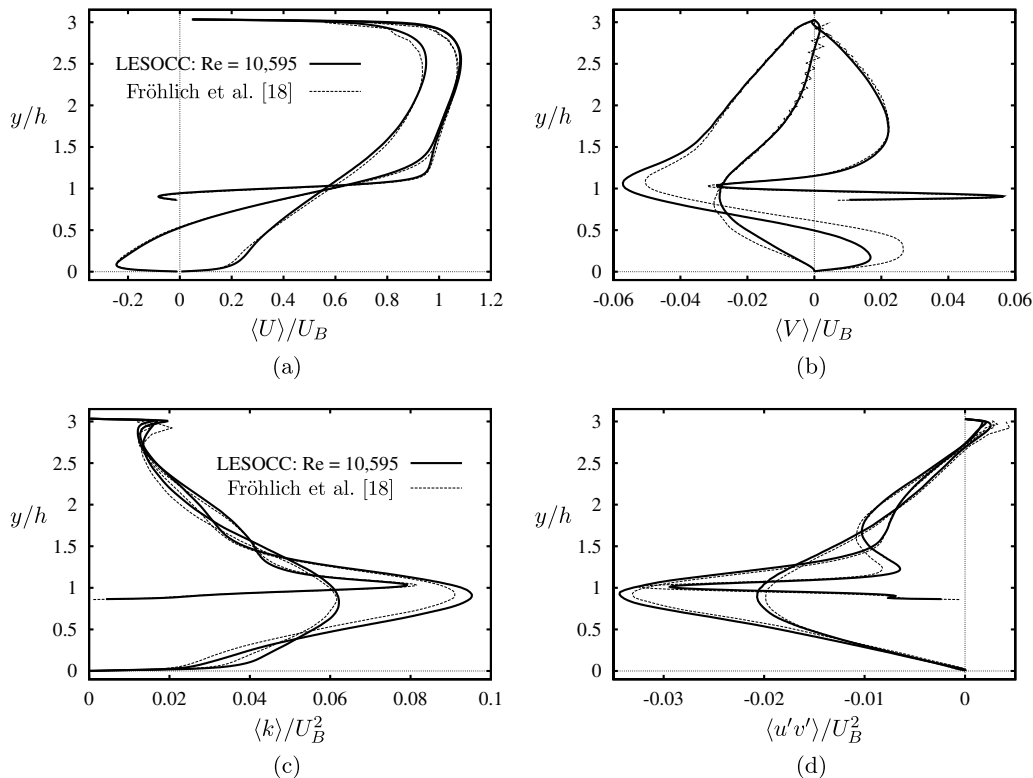

Fig. 17. Comparison of LES predictions by $\mathcal{L}ESOCC$ at $Re = 10,595$ (case 9 in Table 3) and literature data [18] at three different locations ($x/h = 0.5$, 2, and 6): (a) streamwise velocity $\langle U\rangle/U_B$; (b) normal velocity $\langle V\rangle/U_B$; (c) resolved turbulent kinetic energy $\langle k\rangle/U_B^2$; (d) resolved shear stress $\langle u'v'\rangle/U_B^2$.

The streamwise velocity component $\langle U \rangle/U_B$ is underpredicted here and shows a non-smooth behavior. The resolution was quite coarse in that case in [18] partially leading to wiggles in the solution as obvious in Fig. 17(b) for the wall-normal velocity component $\langle V \rangle/U_B$. The deficits resulting from the usage of wall functions at the upper wall are also detectable in the turbulent quantities, e.g., the location of the peak value of $\langle k \rangle/U_B^2$ is shifted away from the upper wall and the shear stress profile $\langle u'v' \rangle/U_B^2$ strongly deviates from the wall-resolved LES prediction (case 9) in this region. Since the total mass flux through the channel was fixed, the underprediction of $\langle U \rangle/U_B$ in the vicinity of the upper wall has a certain influence on the overall flow development. Nevertheless, the agreement between the present wall-resolved LES prediction (case 9) and the literature data [18] is satisfactory and further validates the former.

4.3. Comparison between experimental and numerical results at Re = 5600 and 10,595

Finally, the experimental data at two different Reynolds numbers ($Re = 5600$ and 10,595) are compared with the most accurate predictions. At $Re = 5600$ the DNS data achieved by $\mathcal{MGLET}$ (case 8 in Table 3) are taken into account, whereas at $Re = 10,595$ the highly resolved LES carried out by $\mathcal{LESOCC}$ (case 9 in Table 3) is considered. Fig. 18 depicts averaged velocity profiles for $\langle U \rangle/U_B$ and $\langle V \rangle/U_B$ at four streamwise positions of $x/h = 0.5, 2, 4,$ and 6. Regarding the mean streamwise velocity $\langle U \rangle/U_B$ the agreement between predictions and measurements is very good for both Reynolds numbers. Minor deviations are solely visible in the region of the shear layer where the measurements show slightly higher velocities and in the post-reattachment region where the experimental data exhibit a faster recovery. As observed before, the vertical velocity component $\langle V \rangle/U_B$ is about one order of magnitude smaller than the streamwise component and thus more sensitive.

Nevertheless, the match between experiments and simulations is fully satisfactory. The largest deviations are found at $x/h = 2$, whereas all other profiles exhibit a closer agreement. It should be noted here that regarding the minor deviations found the same trend is observed for both Re independent of the simulation method applied which indicates some systematic reason for this behavior.

Furthermore, the measurements and predictions should be compared with respect to the Reynolds stresses. In the following the experimental data at $Re = 10,595$ are taken into account and compared to the LES prediction (case 9, see Table 3). For that purpose, Fig. 19 displays the three measured components of the Reynolds stress tensor at three different locations ($x/h = 0.5, 2,$ and 6). Looking at the streamwise Reynolds stress (Fig. 19(a)), the measured and predicted data are found to be in close agreement at $x/h = 0.5$ and 2. Solely in the post-reattachment region at $x/h = 6$ the measured peak values of $\langle u'u' \rangle/U_B^2$ are at most 10% higher than in the predictions. Nevertheless, the location of the peak values and the distributions itself are in close accordance with the predictions. The vertical Reynolds stress $\langle v'v' \rangle/U_B^2$ depicted in Fig. 19(b) shows even a better agreement than the streamwise component. In case of the Reynolds shear stress $\langle u'v' \rangle/U_B^2$ (Fig. 19(c)) the deviations observed are of similar magnitude as for the vertical component. Nevertheless, the agreement between the PIV measurement and the LES prediction is highly satisfactory.

During the measurements it was found that the determination of the stresses is getting more and more challenging with decreasing Re. For the case of $Re = 5600$ it leads to the outcome that the profiles of the Reynolds stresses are similarly shaped, but the experimentally determined stresses exceed the numerical ones (case 8 in Table 3) systematically. Pump fluctuations were considered to be the reason for that, but high-pass filtering excluded this cause.
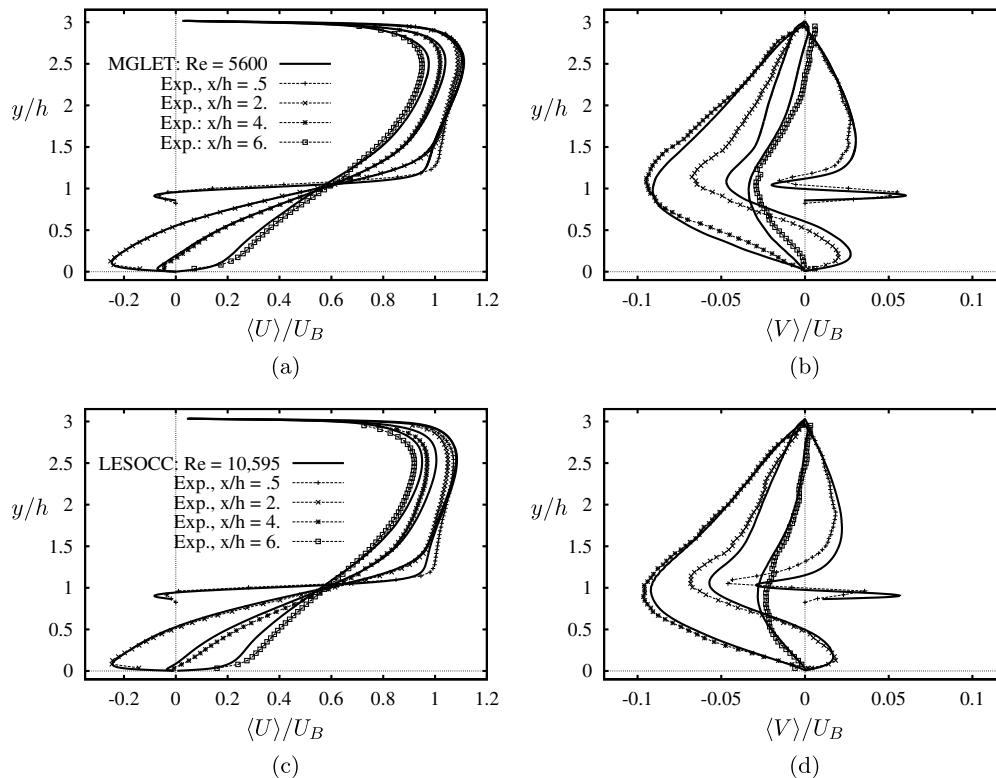

Fig. 18. Comparison of measurements and predictions (case 8 for $Re = 5600$ and case 9 for $Re = 10,595$, see Table 3) at four different locations ($x/h = 0.5, 2, 4,$ and 6): (a) $\langle U \rangle/U_B$ at $Re = 5600$; (b) $\langle V \rangle/U_B$ at $Re = 5600$; (c) $\langle U \rangle/U_B$ at $Re = 10,595$; (d) $\langle V \rangle/U_B$ at $Re = 10,595$.

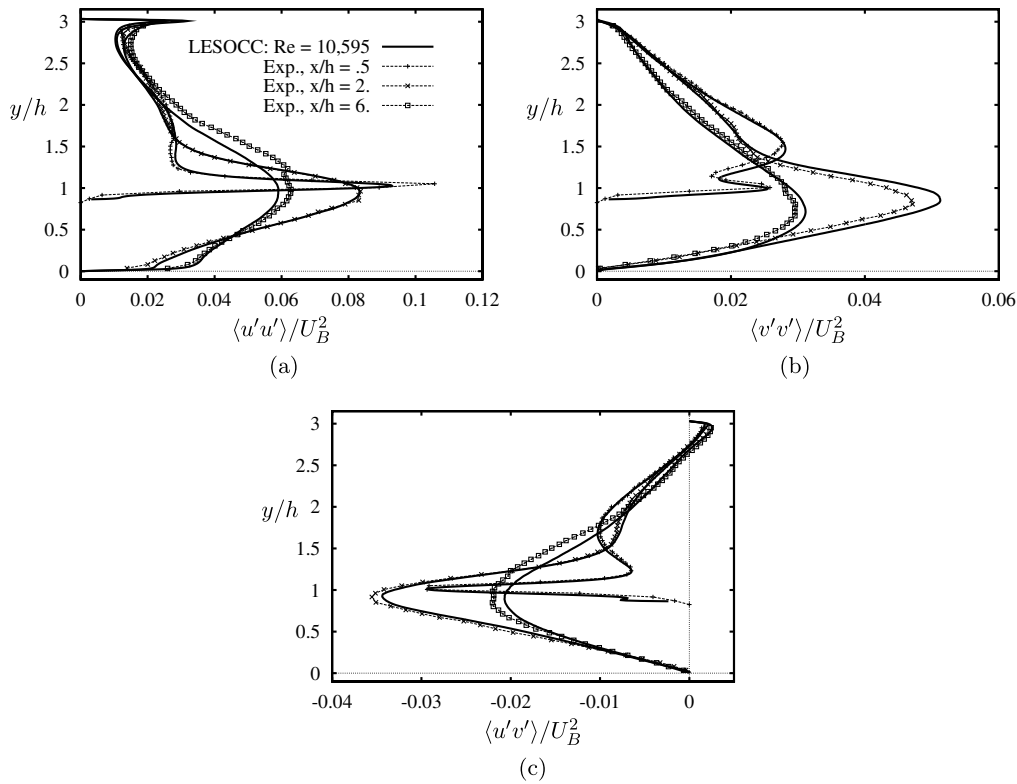Fig. 19. Comparison of measurements and predictions (case 9, see Table 3) for $Re = 10,595$, at three different locations $x/h = 0.5$, 2, and 6.

In conclusion, the variety of cross-comparisons carried out have demonstrated that the predicted data are reliable.

5. Influence of the Reynolds number

After the extensive validations carried out in the previous sections (i.e., CFD vs. CFD, CFD vs. literature, CFD vs. experiment), in the following the flow over periodic hills will be investigated in wide range of Reynolds numbers, i.e., $100 \leqslant Re \leqslant 10,595$. Based on this series of simulations, some peculiar features of the flow field become evident. Here, the evolution and existence of physical phenomena with respect to the Reynolds number is documented. The investigation starts with an overview over the global flow field based on averaged integral quantities such as the wall shear stress and pressure distribution along the lower wall. Then the flow development is studied based on the averaged flow field and the distribution of the Reynolds stresses leading to an investigation on the anisotropy of the flow. Furthermore, the length scales occurring at varying Re will be analyzed. Finally, the instantaneous dynamic behavior of the flow will be considered which will shed more light onto the flow structures and mechanism involved.

5.1. Global averaged properties

A global view of the flow for the lowest as well as the highest Reynolds number investigated is given by the distribution of the averaged streamwise velocity $\langle U \rangle/U_B$ and the streamlines of the averaged flow in Fig. 20. Obviously, the flow field does not change dramatically within this Re range. The recirculation bubble at $Re = 10,595$ is smaller and slightly thinner than at $Re = 700$. Furthermore, the back-flow velocity increases with increasing Re. It is noteworthy to recall that at $Re = 700$ the plane channel flow without constrictions would definitely be in the laminar regime what is unambiguously not the case here.
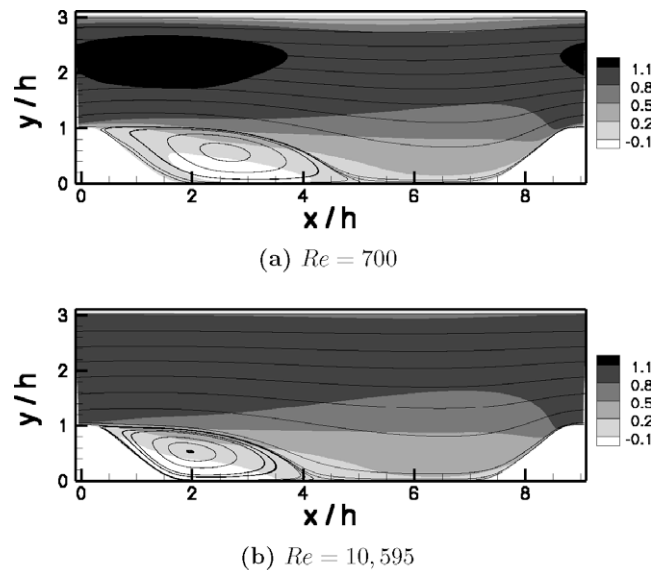

Fig. 20. Comparison of averaged streamwise velocity $\langle U \rangle/U_B$ and streamlines at two different Reynolds numbers ($Re = 700$ and 10,595).

Fig. 21(a) displays the distribution of the wall shear stress τ_w on the lower wall for all Reynolds numbers. Based on this comparison of the DNS and the well-resolved LES predictions, the dependence of τ_w on Re can be clearly appreciated.

The first observation is that the peak values of τ_w strongly increase with decreasing Re. That is obvious for the values found at the hill crest ($x/h = 0$), the minimum in the recirculation region ($x/h \approx 2$–5), and the maximum at the shoulder of the second hill ($x/h \approx 8.6$). The increase is monotonous but non-linear with Re.
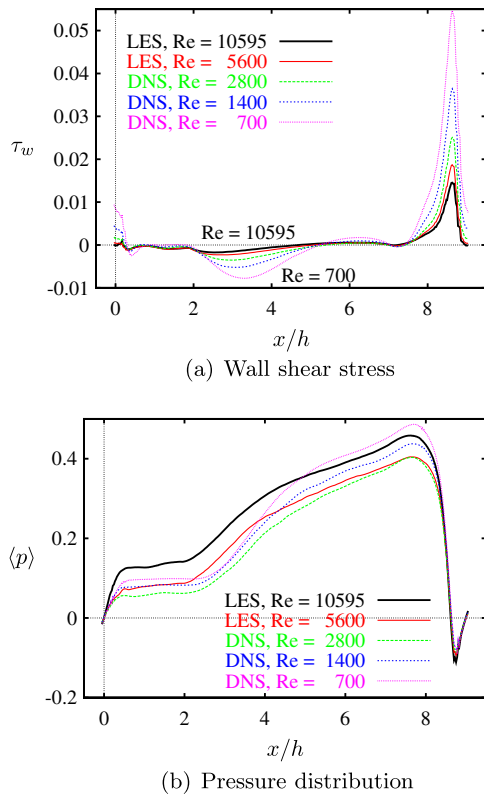
(a) Wall shear stress

(b) Pressure distribution

Fig. 21. Distribution of the averaged wall shear stress τ_w and the averaged pressure distribution $\langle p \rangle$ along the lower wall for five different Reynolds numbers, predictions by $\mathcal{LESOCC}$.

In order to understand this behavior, two contrary effects have to be considered playing an important role. Based on the definition of the wall shear stress $\tau_w = \mu \partial V^{\text{parallel}}/\partial n$ it is on the one hand obvious that τ_w increases with decreasing Re since for fixed U_B and h the viscosity has to increase. On the other hand the velocity gradient at the wall is decreasing when Re is reduced as will be shown in the next section. Thus both opposite influences are superimposed yielding this non-linear behavior.

The flow separates shortly behind the hill crest at all Re. As shown in Fig. 22 the separation point moves upstream from $x_S/h \approx 0.45$ at $Re = 100$ to $x_S/h \approx 0.3$ at $Re = 700$ and finally to $x_S/h \approx 0.18$ at $Re = 5600$ but then settles down at a slightly larger
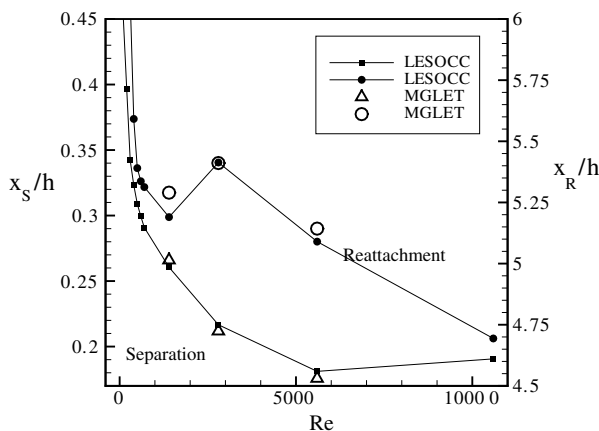
value of $x_S/h \approx 0.19$ at $Re = 10,595$. The undulations in the wall shear stress at the beginning of the main recirculation bubble seem to be geometry related and not much affected by Reynolds number effects. This statement is supported by the observation that the undulations are visible in all simulations using $\mathcal{LESOCC}$ but also for the predictions based on $\mathcal{MGLET}$ (compare Fig. 11(a)).

Past the hill the main recirculation region follows with a nearly constant pressure plateau in a large part of the separation bubble (Fig. 21(b)). The reattachment position x_R/h displayed in Fig. 22 decreases from $Re = 100$ to 1400. Between $Re = 1400$ and $Re = 2800$ a sudden change can be observed in Fig. 22. The reattachment length x_R/h increases again in this narrow Re-range. Afterwards, a clear trend concerning the reattachment length is visible for $Re \geqslant 2800$ where x_R/h decreases again with increasing Re. Since this phenomenon is consistently predicted by both independent codes, it is assumed to be no numerical artifact. The corresponding values of the reattachment lengths are $x_R/h = 5.24, 5.19, 5.41, 5.09$, and 4.69 for $Re = 700$ to 10,595, respectively. A similar behavior of the reattachment length with increasing Re has been observed for the backward-facing step flow by Armaly et al. [3]. This observation also explains why with increasing Re there is no continuous trend visible for the averaged pressure distribution depicted in Fig. 21(b).

Interestingly, a small region with positive averaged wall shear stress is found within the main separation bubble at $Re = 1400$ by both codes (case 2 and 3). That leads to a tiny counterclockwise rotating structure in the region $x/h \approx 0.6$–0.8 at the falling edge of the hill which is depicted in Fig. 23. Contrarily, at the higher Re numbers τ_w is negative in the entire recirculation region and thus no such tiny structure is detected. This special feature solely observed at $Re = 1400$ might be an explanation for the non-monotonous behavior of the reattachment length x_R/h. However, the interpretation has to be done with care, since one has to bear in mind that the data presented are averaged in time and in homogeneous direction. Animations of the flow field at the low Reynolds number cases have clearly shown that along the falling edge of the hill intermittently attached flow regions can be detected which explain the positive wall shear stress.

In the post-reattachment zone a tiny recirculation region is detected in front of the second hill at $x/h \approx 7.0$–7.4. This feature is found for all $Re > 200$ investigated, but again the largest extension of this structure is observed at $Re = 2800$ (see Fig. 24). On the windward side of the second hill the flow is strongly accelerated (see also Fig. 21(b) for the pressure distribution) leading to a distinctive peak of τ_w shortly before the hill crest at $x/h \approx 8.6$. The peak value of τ_w significantly increases with decreasing Re. Downstream of that position the pressure gradient suddenly changes from favorable to adverse yielding a strong drop of the wall shear stress between $x/h \approx 8.6$–9.0 for all Re. At the hill crest, just before

Fig. 22. Separation length and reattachment length vs. Reynolds number; comparison of predictions by $\mathcal{LESOCC}$ and $\mathcal{MGLET}$ (values for $Re < 700$ are based on coarse-grid simulation mentioned in Section 5.5).
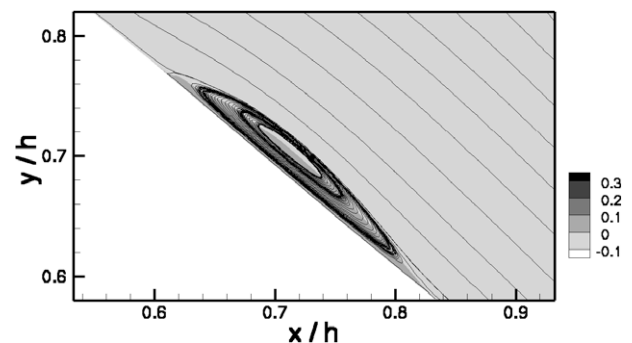

Fig. 23. Tiny bubble with positive averaged wall shear stress found within the main recirculation region at the falling edge of the hill at $Re = 1400$ visualized by the averaged streamwise velocity $\langle U \rangle/U_B$ and streamlines.
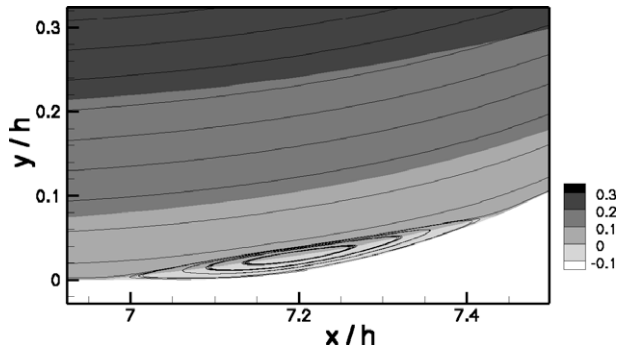
Fig. 24. Tiny recirculation bubble in front of the second hill at $Re = 2800$ visualized by the averaged streamwise velocity $\langle U \rangle / U_B$ and streamlines.

the main separation, a tiny recirculation zone forms solely at the highest Re. This phenomenon was not observed before. It is unlikely that it is an artifact because a clear downwards trend of the

wall shear stress with increasing Re definitely supports this observation. Furthermore, an additional simulation at $Re = 22,400$ (not shown here) assists the decreasing τ_w at $x/h \approx 0$ and thus delivers further evidence. It should be noted in this context that right on the hill crest the boundary is flat.

An explanation for this tiny recirculation zone in the averaged flow field can be found in the instantaneous data. Irregularly the flow in the vicinity of the hill crest already separates at $x/h \approx 8.8$ generating additional eddies. These partially strong eddies are transported downstream and affect the flow supposed to separate on the curved wall. Therefore, also the separation on the leeward side is strongly influenced by the flow phenomena appearing before or at the crest. Since this early separation before the hill crest is only detected temporarily, it is hardly visible in the averaged flow field.

5.2. Averaged velocity and Reynolds stress profiles

In this section certain positions in the flow will be investigated more closely. For that purpose the mean flow velocities $\langle U \rangle / U_B$ and
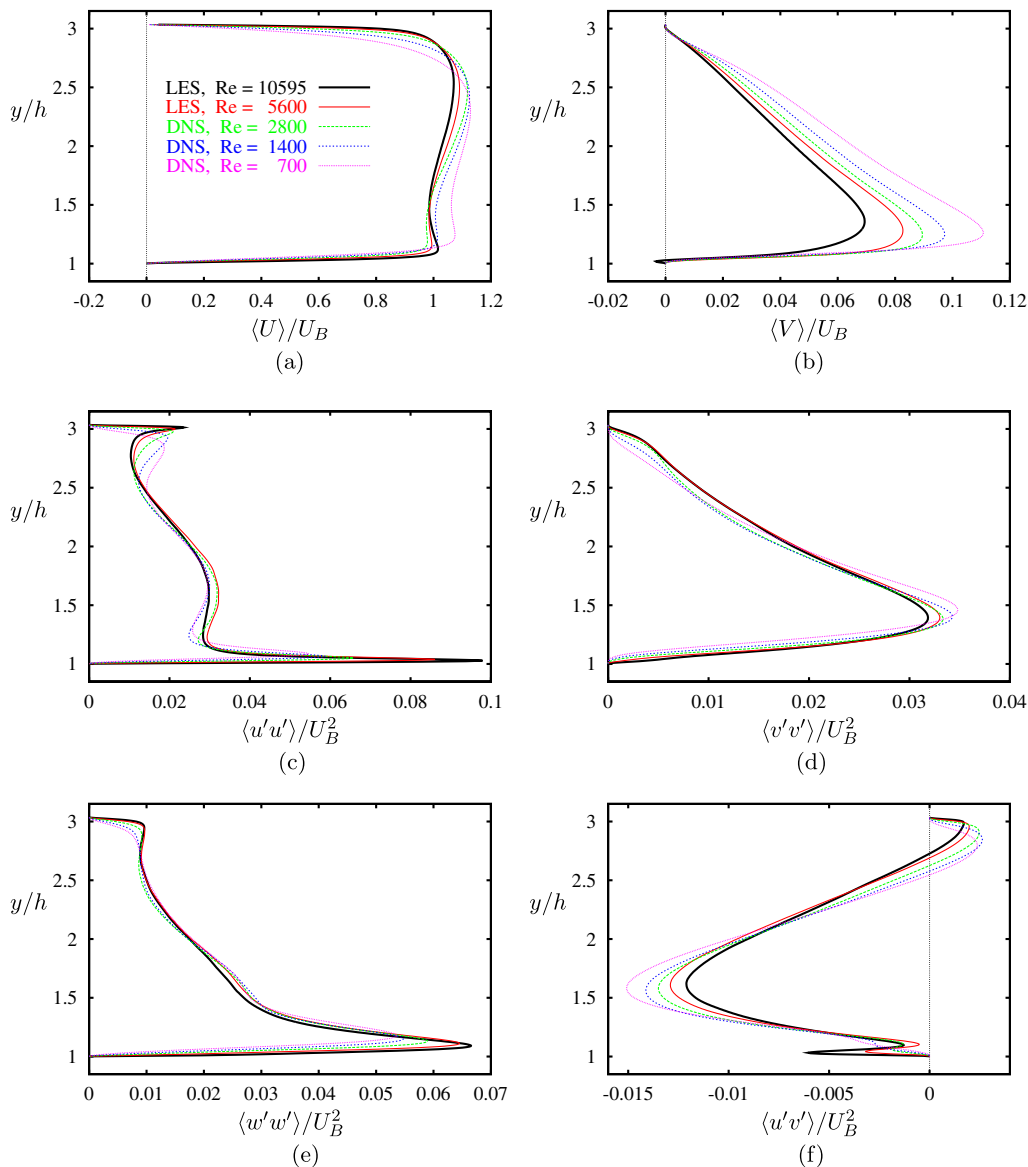

Fig. 25. Profiles of the streamwise velocity $\langle U \rangle / U_B$, the normal velocity $\langle V \rangle / U_B$, and the resolved Reynolds stresses $\langle u'u' \rangle / U_B^2$, $\langle v'v' \rangle / U_B^2$, $\langle w'w' \rangle / U_B^2$, and $\langle u'v' \rangle / U_B^2$ at position $x/h = 0.05$ for five different Reynolds numbers, predictions by $\mathcal{LESOCC}$.

$\langle V \rangle / U_B$ as well as all non-zero Reynolds stresses are depicted at four locations, i.e., $x/h = 0.05$ (close to the hill crest), $x/h = 2$ (in the middle of the main recirculation region), $x/h = 4$ (close to the end of the main recirculation region), and $x/h = 8$ (at the windward side of the second hill). The corresponding plots can be found in Figs. 25–28.

It is visible at all positions shown that on both walls the velocity gradients of $\langle U \rangle / U_B$ increase with increasing Re and owing to a fixed mass flow rate the maximum of the streamwise velocity is decreasing (compare also Fig. 20). The change in the slope can be seen most clearly at the upper wall. Furthermore, the back-flow velocity in the middle of the main recirculation region ($x/h = 2$) increases with increasing Re and overall the recirculation bubble becomes slightly thinner. A clear trend is also obvious for $\langle V \rangle / U_B$. For example at $x/h = 0.05$ the maximum and at $x/h = 4$ the minimum significantly increase with decreasing Re, respectively.

Concerning the Reynolds stresses the following observations can be made. At the beginning of the free shear layer at $x/h = 0.05$ the peak value of $\langle u'u' \rangle / U_B^2$ is strongest at $Re = 10,595$, whereas only about half of the strength is found at $Re = 700$. The fluctuations in

wall-normal direction $\langle v'v' \rangle / U_B^2$ are, however, of the same size for all Re. Since the development of the free shear layer is shifted downstream for decreasing Re (see Fig. 29), similar peak values of $\langle u'u' \rangle / U_B^2$ and $\langle u'v' \rangle / U_B^2$ are already observed at $x/h = 2$ for all Re. Thus these extrema appearing in the free shear layer are approximately independent of Re. Furthermore, with increasing Re the positions of the extrema are shifted closer to the lower wall which is in accordance with the thinner recirculation region mentioned above. The size of the peak values of the two other Reynolds stresses $\langle v'v' \rangle / U_B^2$ and $\langle w'w' \rangle / U_B^2$, however, decrease with decreasing Re.

Another clear trend can be seen for the free shear layer which broadens with increasing Re. That is obvious in the distribution of all Reynolds stresses depicted in Fig. 26 at $x/h = 2$. Moreover, the peak values of $\langle u'u' \rangle / U_B^2$ and $\langle w'w' \rangle / U_B^2$ in the vicinity of the upper wall increase with increasing Re and move closer to the walls as expected for a turbulent flow in the vicinity of a plane wall.

Close to the end of the recirculation bubble at $x/h = 4$ and past the bubble at $x/h = 6$ (not shown here) the situation is different. Here, the peak values of $\langle u'v' \rangle / U_B^2$ increase strongly with decreasing
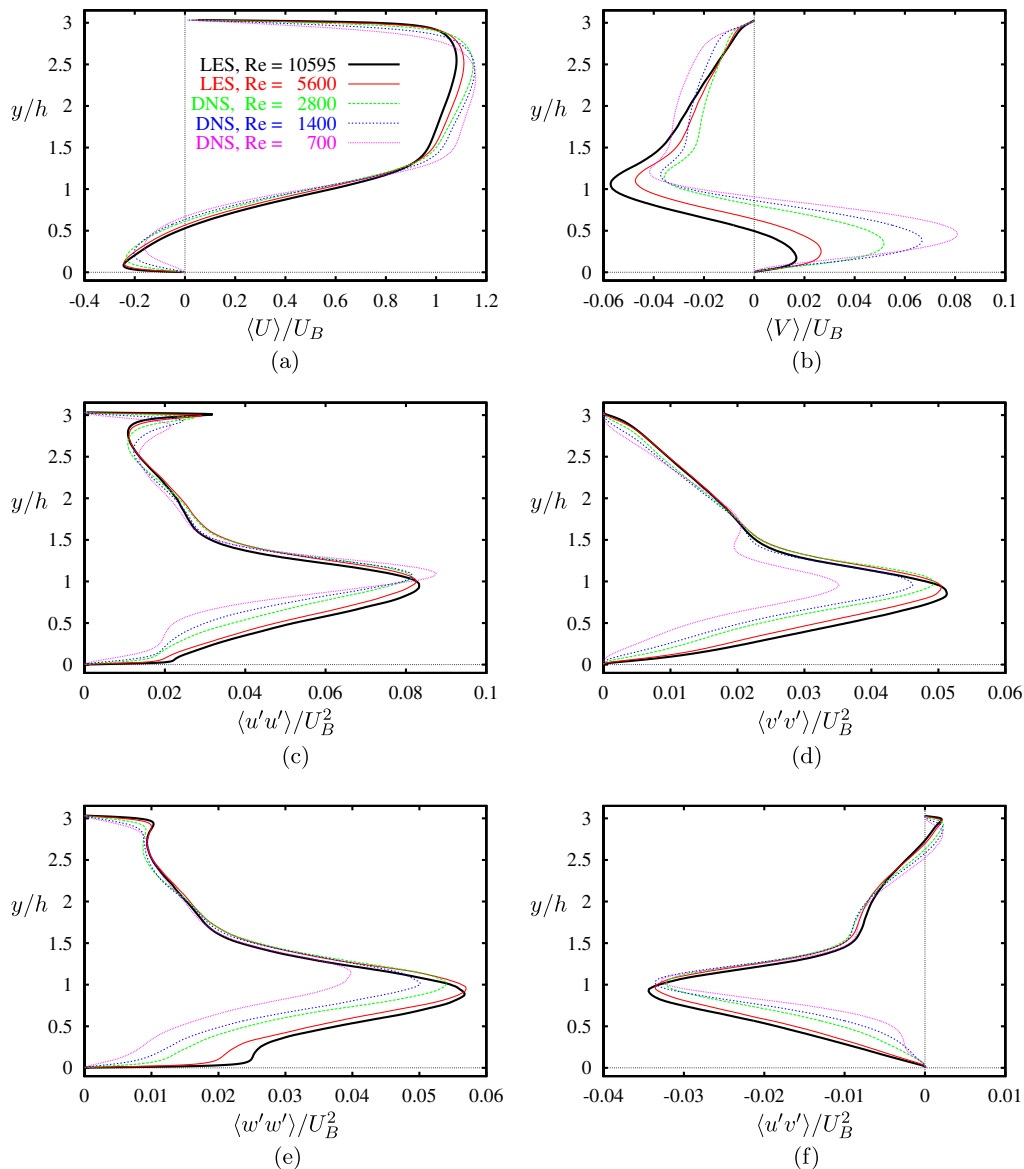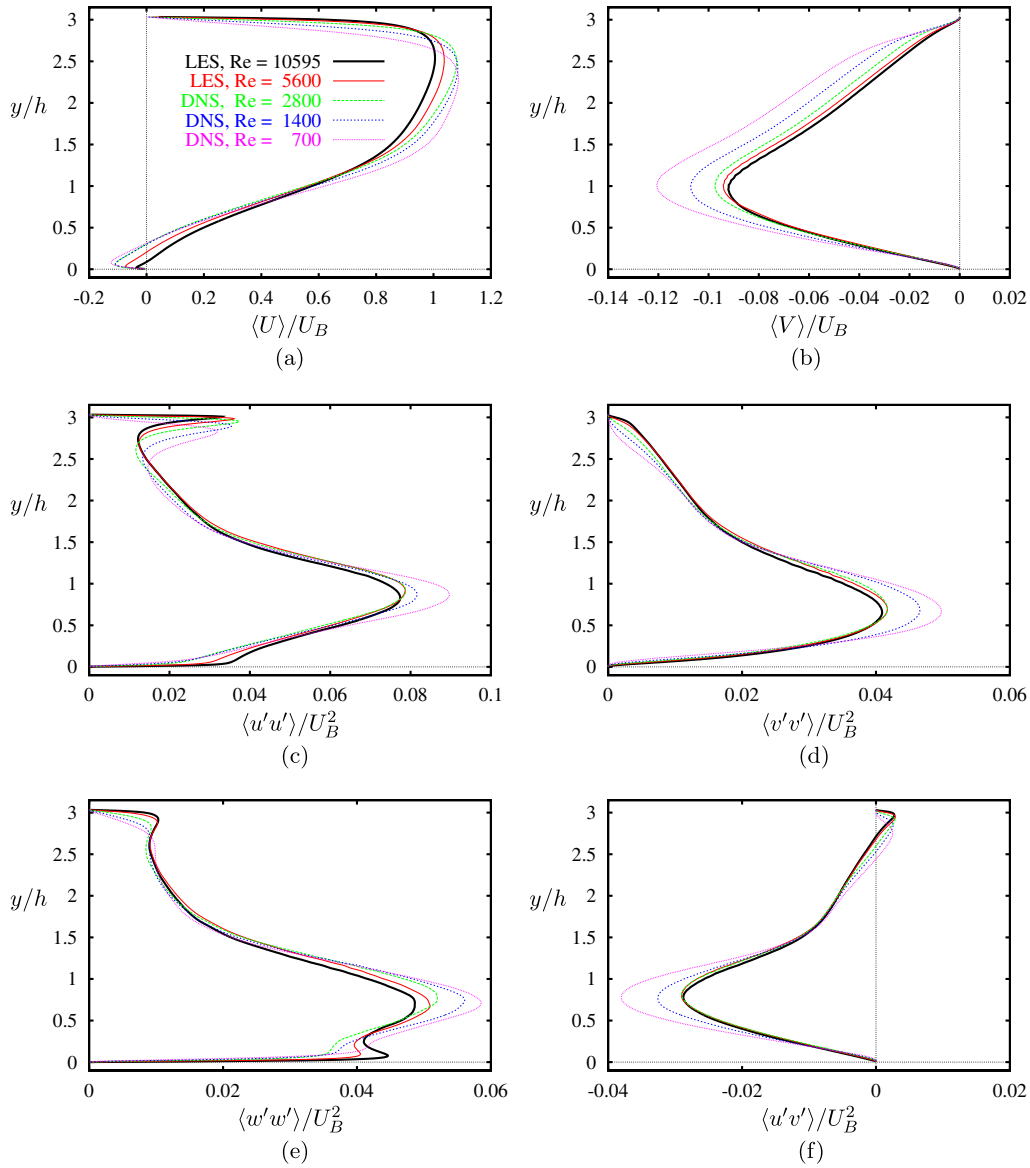

Fig. 26. Profiles of the streamwise velocity $\langle U \rangle / U_B$, the normal velocity $\langle V \rangle / U_B$, and the resolved Reynolds stresses $\langle u'u' \rangle / U_B^2$, $\langle v'v' \rangle / U_B^2$, $\langle w'w' \rangle / U_B^2$, and $\langle u'v' \rangle / U_B^2$ at position $x/h = 2.0$ for five different Reynolds numbers, predictions by $\mathcal{L}$ESOCC.

Fig. 27. Profiles of the streamwise velocity $\langle U \rangle/U_B$, the normal velocity $\langle V \rangle/U_B$, and the resolved Reynolds stresses $\langle u'u' \rangle/U_B^2$, $\langle v'v' \rangle/U_B^2$, $\langle w'w' \rangle/U_B^2$, and $\langle u'v' \rangle/U_B^2$ at position $x/h = 4.0$ for five different Reynolds numbers, predictions by $\mathcal{L}ESOCC$.

Re. Contrarily to $x/h = 2$ the peak values of all normal Reynolds stresses at $x/h = 4$ and 6 also increase with decreasing *Re*. An explanation for the opposite behavior found at the different locations can be given based on Fig. 29 which depicts exemplarily the distribution of the turbulent kinetic energy for the lowest and the highest Reynolds number investigated. This comparison clearly shows that the peak values of $\langle k \rangle/U_B^2$ are of similar size at both *Re* but shifted downstream for the low-*Re* case compared with the high-*Re* case. Thus, lower fluctuations are found for example at $x/h = 2$ for $Re = 700$ compared with $Re = 10,595$, whereas further downstream larger peak values exist for the low-*Re* flow.

In principle, the same trend as observed at $x/h = 4$ and 6 can also be seen at the windward slope of the second hill, i.e., at $x/h = 8$. The most interesting feature is here the observation that the maximum of the spanwise Reynolds stress $\langle w'w' \rangle/U_B^2$ in the vicinity of the wall is nearly independent of the Reynolds number. As discussed in [18] this phenomenon reveals to be the result of the 'splatting' of large-scale eddies originating from the shear layer and convected downstream towards the windward slope. Thus, the distribution of $\langle w'w' \rangle/U_B^2$ in Fig. 28(e) delivers a clear hint that the

same mechanism must play an important role also for the lowest Reynolds number considered. Consequently, the phenomenon has to be nearly independent of *Re*. That explains why the distributions of the mean velocities and Reynolds stresses are very similar close to the windward slope of the second hill at $x/h = 8$.

5.3. Anisotropy-invariant investigations

Lumley and Newman [27] and Lumley [28] found that the state of turbulence can be characterized by the amount of anisotropy that prevails in the flow. The anisotropy of a flow can be derived from the Reynolds stresses $\tau_{ij} = -\rho \langle u_i u_j \rangle$ by subtracting the isotropic part from τ_{ij} and normalizing with $\tau_{ss} = -\rho \langle u_s u_s \rangle$. This leads to the non-dimensional anisotropy tensor

$$a_{ij} = \frac{\langle u_i u_j \rangle}{2 \langle k \rangle} - \frac{1}{3} \delta_{ij}, \tag{6}$$

with the turbulent kinetic energy $\langle k \rangle = 1/2 \langle u_s u_s \rangle$ and the Kronecker delta δ_{ij}. The tensor a_{ij} has three scalar invariants:
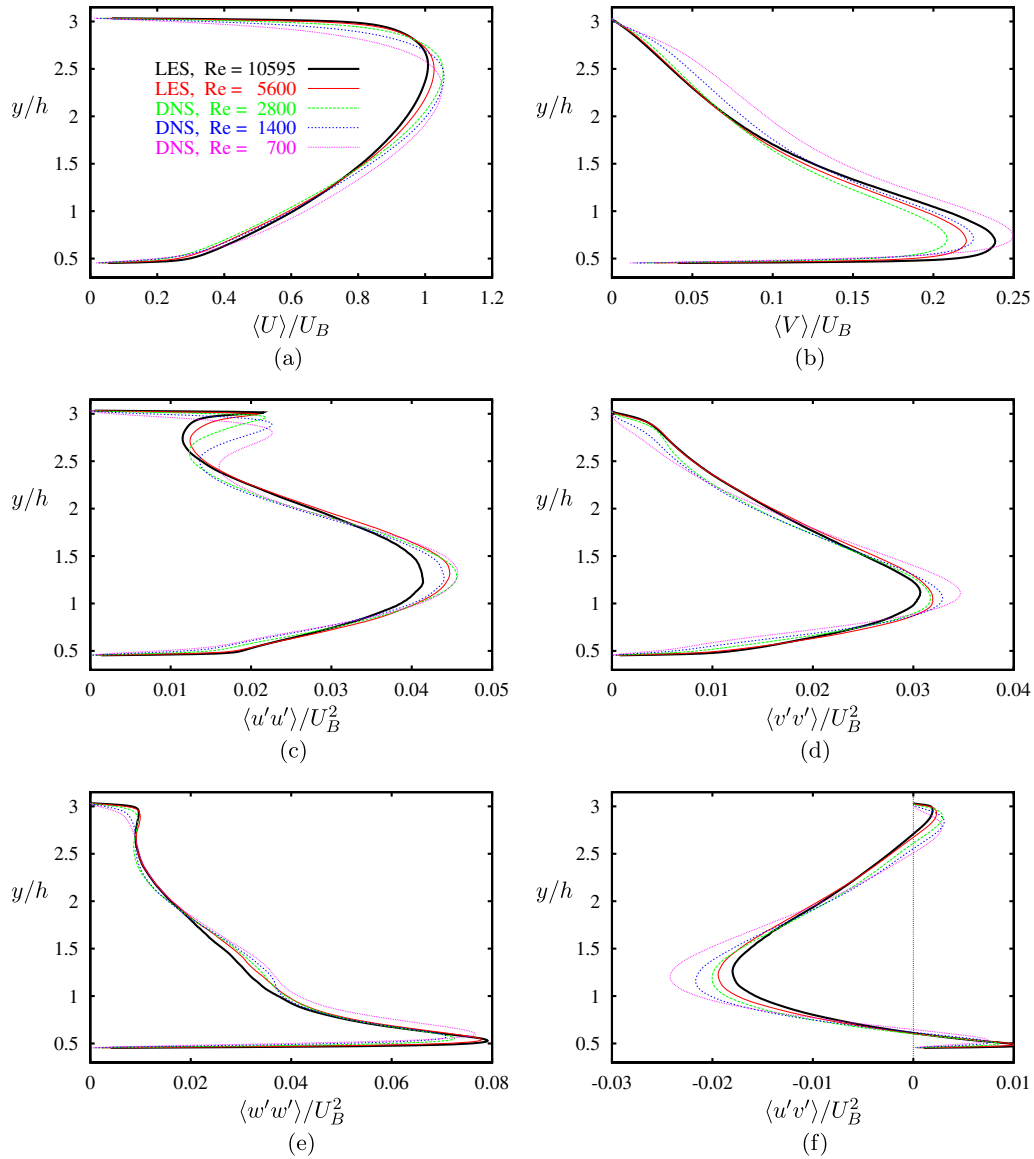
Fig. 28. Profiles of the streamwise velocity $\langle U \rangle / U_B$, the normal velocity $\langle V \rangle / U_B$, and the resolved Reynolds stresses $\langle u'u' \rangle / U_B^2$, $\langle v'v' \rangle / U_B^2$, $\langle w'w' \rangle / U_B^2$, and $\langle u'v' \rangle / U_B^2$ at position $x/h = 8.0$ for five different Reynolds numbers, predictions by $\mathcal{L}ESOCC$.

$$a_{ii} = 0, \quad \text{II} = a_{ij}a_{ji}, \quad \text{III} = a_{ij}a_{jk}a_{ki}. \tag{7}$$

By cross-plotting II and III, the state of turbulence in a flow can be displayed with respect to its anisotropy. If the scalar invariants II and III are evaluated for the case of a two-component turbulence (one component of the velocity fluctuations is negligibly small compared with the other two), this leads to II = 2/9 + 2III. Doing the same for the axisymmetric turbulence (two components are equal in magnitude) yields II = 3/2(4/3|III|)²/³. Hence, if these relations are cross-plotted as done in Fig. 30, they define a narrow region called the *anisotropy-invariant map*. It was shown by Lumley [28] that all physically realizable turbulence has to lie within this small region. However, different states of turbulence are represented by different parts of the map.

The boundaries of the invariant map describe the limiting states of turbulence [24]. Isotropic turbulence is found at the lower corner point of the map (origin in Fig. 30) where II = III = 0, hence the anisotropy is zero. The left branch of the map (III < 0) describes axisymmetric turbulence in which one component of the velocity fluctuations is smaller than the other two. In the literature, this

is sometimes referred to as 'pancake' type of turbulence. The simplest example of this type is the passage of grid turbulence through axisymmetric contraction. In contrast, the axisymmetric turbulence on the right side (III > 0) is characterized by one fluctuating component which dominates over the other two. This, for example, holds for grid turbulence through axisymmetric expansion and is called 'cigar'-like turbulence. The remaining boundary line on top of the map is the limiting case of a two-component turbulence as it can be found in the direct vicinity of walls. Here, the wall-normal component of the velocity fluctuations is tending towards zero, leaving only the wall-parallel components. The corner point on the left-hand side of the anisotropy-invariant map represents a turbulence state in which only two fluctuating components of equal intensity exist called two-component isotropic turbulence. Finally, the right top end of the map describes one-component turbulence, which consists merely of one fluctuating component.

In order to compare the lowest and the highest Reynolds number regarding the anisotropy of turbulence, Fig. 30 displays the states of turbulence along four streamwise locations in the flow field, namely x/h = 2, 4, 6, and 8. The points at the upper and lower
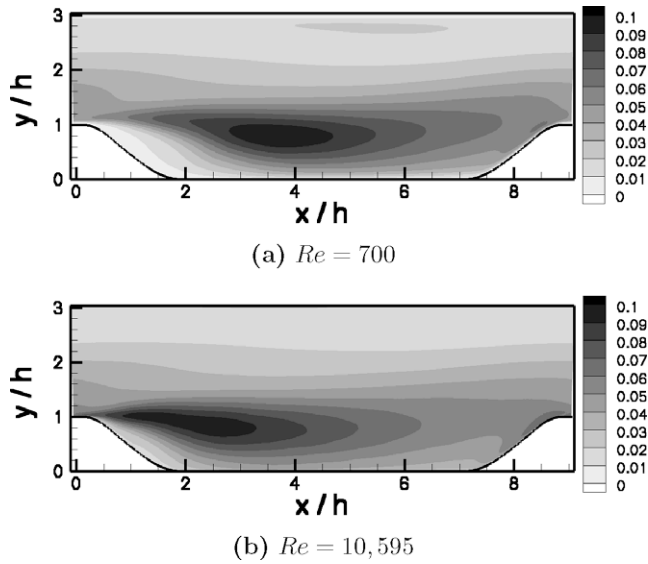
(a) $Re = 700$

(b) $Re = 10,595$

Fig. 29. Comparison of turbulent kinetic energy $\langle k \rangle / U_B^2$ at two different Reynolds numbers ($Re = 700$ and 10,595).

wall are denoted by 'U' and 'L', respectively. First, it has to be remarked that taking the entire flow into account all states indeed lie within the invariant map (not shown here), as it is required by realizability constraints. Second, as requested, the end points of the streamwise profiles at both walls are found at the two-component limit for both Re. At the upper wall the anisotropy is larger for $Re = 10,595$ than for $Re = 700$ and thus the U-point at all locations considered is shifted to the right towards the one-component limit. Contrarily, at the lower wall the L-point is shifted to the left towards the two-component isotropic limit at $Re = 10,595$ in comparison with $Re = 700$. In the vicinity of the upper wall the well-known behavior of the invariants for a plane channel flow can be observed, i.e., progressing along the 'axisymmetric expansion' line in the log-region towards the one-component limit and settling down at the two-component limit at the wall. The main difference between both Re is given by larger extrema found at $Re = 10,595$.

When approaching the lower wall at $x/h = 2$ a fundamental deviation is found for both Re. In the high-Re case the approach occurs mostly along the 'axisymmetric contraction' line (III < 0), whereas for the low-Re case the approach is closer to the 'axisymmetric expansion' line (III > 0). However, looking at the situation further downstream ($x/h = 4$) in the region of the main recirculation bubble, the trace in the anisotropy-invariant map is similar for both Re.
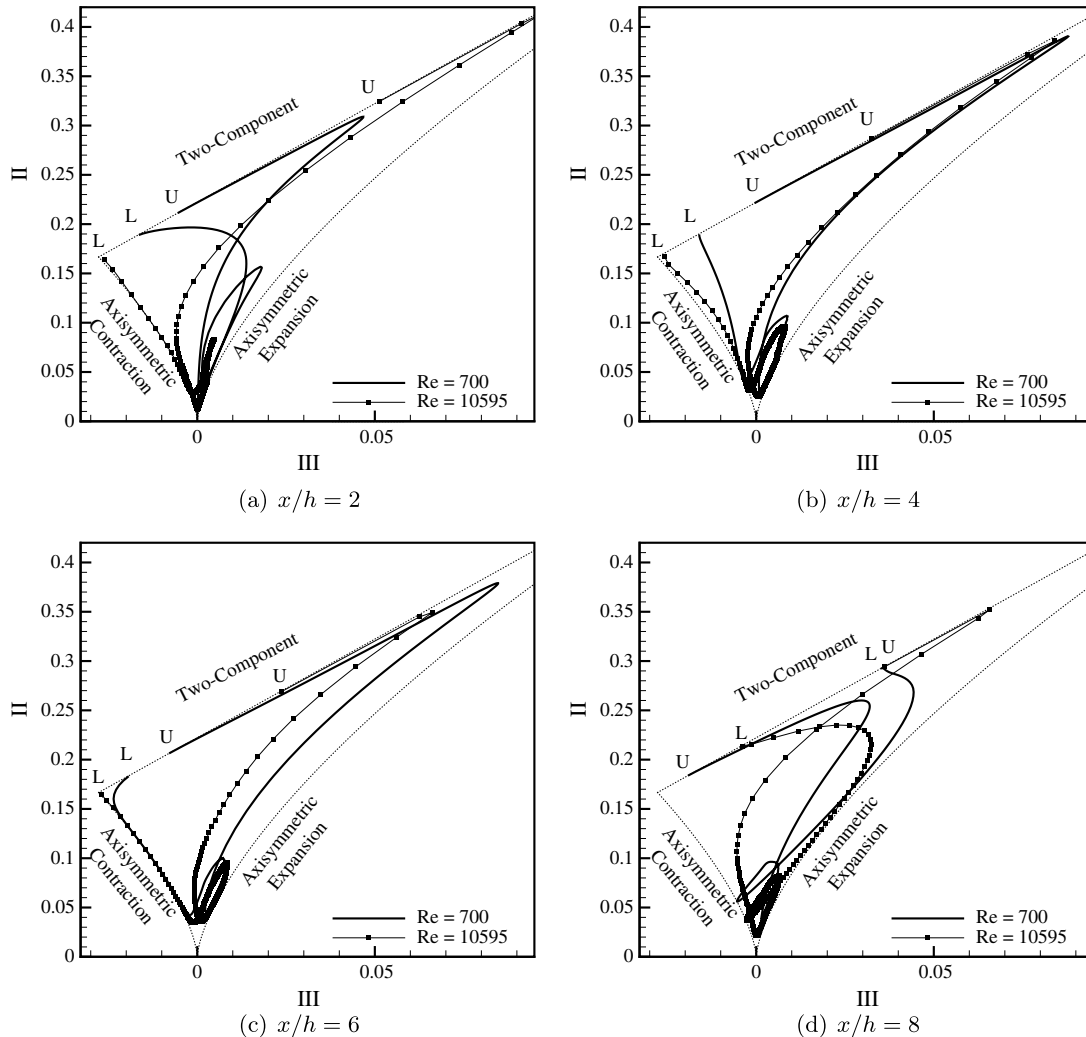

(a) $x/h = 2$

(b) $x/h = 4$

(c) $x/h = 6$

(d) $x/h = 8$

Fig. 30. Anisotropy-invariant mapping at four streamwise locations and at two different Reynolds numbers ($Re = 700$ and 10,595); 'L' and 'U' denote the end points of the trace at the lower and upper wall, respectively.
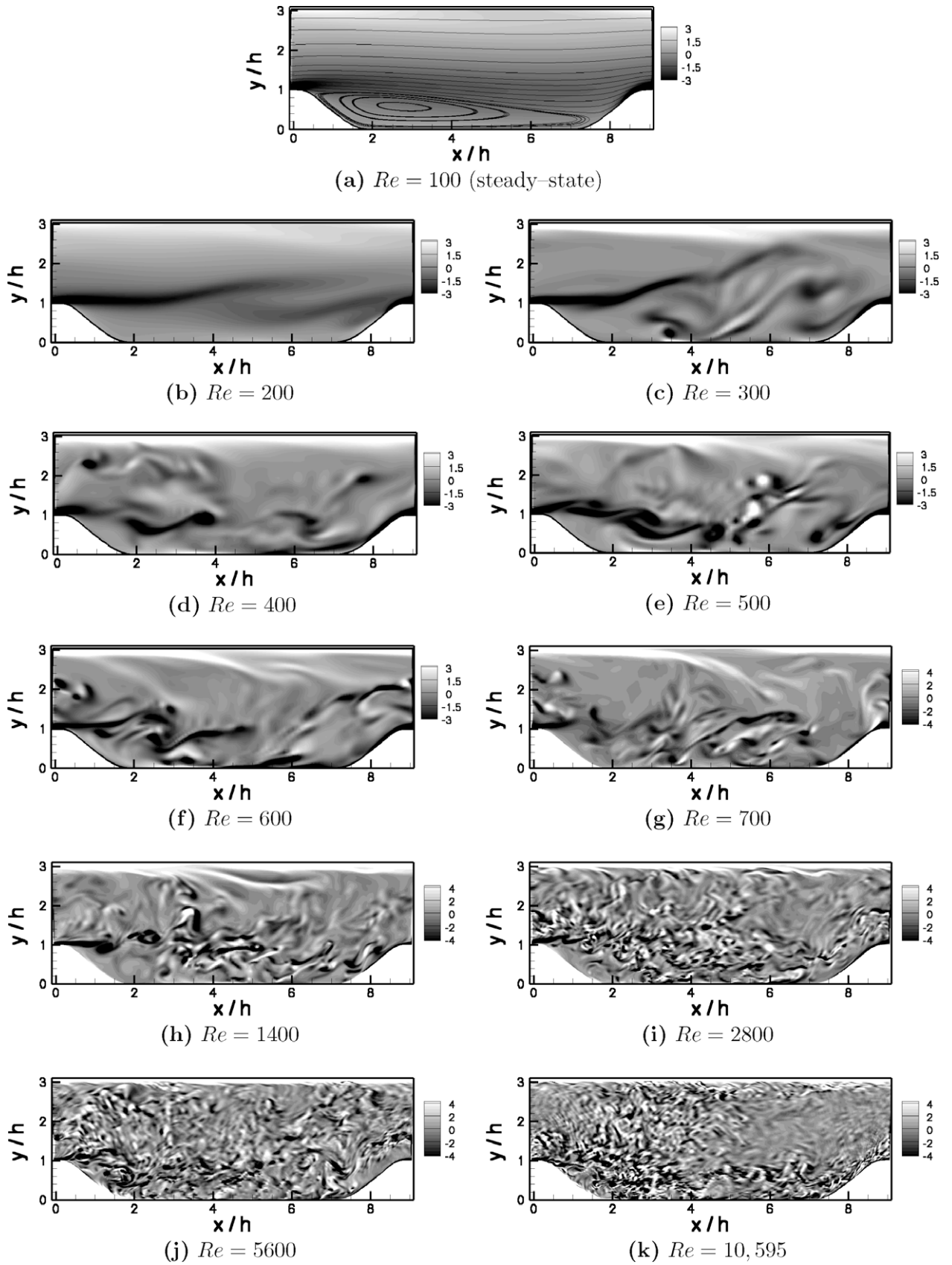
Fig. 31. Comparison of (instantaneous) vorticity component ω_z normal to the cross-section at 11 different Reynolds numbers ($Re = 100$–10,595) at an arbitrarily chosen instant in time; cases (a)–(f) were computed on a coarser grid as described in Section 5.4.

Coming from the area of high anisotropy in the region of the one-component limit (vicinity of the upper wall) with decreasing distance to the lower wall the trace in the invariant map first progresses towards the isotropic limit, nestles against the 'axisymmetric expansion' line and finally comes close to the 'axisymmetric contraction' line stopping at the two-component limit. As mentioned in [18] this signifies a behavior very different from that in a log-law layer of an attached flow. The corresponding end points are at ($Re = 10,595$) or very close to ($Re = 700$) the left corner point of the anisotropy-invariant map, i.e., the two-component isotropic turbulence.

Basically, the same observation can be also made at $x/h = 6$. Thus the qualitative disagreement found at $x/h = 2$ is again resulting from the delayed development of the flow in streamwise direction at $Re = 700$ compared with $Re = 10,595$ as shown in Fig. 29.

At $x/h = 8$ the states of turbulence deviate for the upper part of the computational domain. That is the result of a much thicker boundary layer for the low-Re case (see Fig. 28). However, close to the windward side of the second hill where the flow is strongly accelerated again, the two-component state at the wall itself is approached coming from the 'axisymmetric expansion' line (III > 0) in both cases. That means that one component is dominating over the other two. Reconsidering the profiles of the Reynolds stresses at $x/h = 8$ in Fig. 28, it is clear that the spanwise component $\langle w'w' \rangle$ is substantially larger close to the wall than both other normal Reynolds stresses. That holds for all Re investigated and is a direct result of the 'splatting' effect mentioned above. As shown in [18] for $Re = 10,595$, the pressure–strain correlation in the Reynolds stress equation is the major source of gain for $\langle w'w' \rangle$.

In summary, the anisotropy-invariant map demonstrates that physically similar observations can be made for both Re. Partially, the development is shifted downstream for the low-Re case as seen before leading to disagreements, e.g., at $x/h = 2$. Nevertheless, in spite of more pronounced extrema observed for the high-Re case, the states of turbulence are comparable at both Re.

5.4. Length scales in the flow field

Fig. 31 displays a snapshot of the instantaneous vorticity distribution at an arbitrary instant in time at different Reynolds numbers including a series of Reynolds numbers not mentioned before, i.e., $Re = 100, 200, 300, 400, 500$, and 600. For these low-Re cases it was not necessary to apply the very fine curvilinear grid described in Section 3.4.1. Instead, a body-fitted grid with about 1 million CVs ($164 \times 100 \times 64$) was generated. Comparisons of results obtained on this grid and those of the fine grid at $Re = 700$ served as an evidence that the coarse grid is sufficient to resolve all flow features in this Re range.

The series depicted in Fig. 31 clearly demonstrates how the scales in the flow field become smaller with increasing Re. Based on the well-known relation $\eta/L \sim Re^{-3/4}$ for the Kolmogorov length η describing the smallest length scales in a turbulent flow, the ratio between the length scales at two different Re can be estimated. Assuming that the largest scale L restricted by the geometry stays constant, the maximal ratio of the smallest length scales is about 20 for the instantaneous cases depicted in Fig. 31(b)–(k).

For the low-Re cases the shear layer developing past the hill is distinctively visible followed by the well-known Kelvin–Helmholtz instability. With increasing Re the region where this instability is observed first, moves upstream and comes very close to the hill crest. Furthermore, a lot of small-scale vortices are visible in this area so that the origin of the Kelvin–Helmholtz instability is hardly visible.

5.5. Instantaneous dynamics of the flow

Based on the outcome of Sections 5.1–5.4 which showed that the important flow features are very similar in a wide range of

Reynolds numbers, the idea came up to investigate the dynamics of the flow field first at low Reynolds numbers. The objective is to study the dynamic behavior of the large-scale structures in the flow which at low Re are not overwhelmed by small-scale eddies. Thus structure-identification methods such as the λ_2 criterion by Jeong and Hussain [23] can be applied to the low-Re cases involved.

As mentioned above, for that purpose additional simulations were carried out at a series of Reynolds numbers in the range $100 \leqslant Re \leqslant 700$ using a curvilinear grid with about 1 million CVs. All simulations were started from scratch with two-dimensional initial conditions defined by $U/U_B = 1$ (except at the walls) and $V/U_B = W/U_B = 0$.

At the lowest Reynolds number considered, i.e., $Re = 100$, the flow is found to reach steady-state after about 100 dimensionless time units which is equivalent to about 11 flow-through times (see Fig. 31(a)). The flow separates past the hill crest at about $x/h = 0.45$ and forms a large recirculation region which fills the lower portion of the entire constriction completely. Thus reattachment is observed in this case at the rising edge of the second hill at about $x/h = 7.73$. No three-dimensional structures can be detected.

The situation changes completely when the Reynolds number is increased to $Re = 200$ (Fig. 31(b)). Now and for all other higher Re the flow remains unsteady all the time. Up to about 140 dimensionless time units the flow field at $Re = 200$ is two-dimensional. However, after this initial phase first three-dimensional flow structures develop which are detected by monitoring the spanwise velocity component W. With increasing Re the initial two-dimensional stage is shortened so that at $Re = 700$ first three-dimensional phenomena can be found at about 50 dimensionless time units past the initial stage. The corresponding snapshots of the instantaneous vorticity distribution at an arbitrary instant at all low-Re cases considered are displayed in Fig. 31(a)–(g).

Fig. 32 displays one-dimensional spectra of the spanwise velocity component W recorded for a point close to the rising slope of the second hill ($x/h = 8.3$; $y/h = 0.72$). The frequency f is normalized by U_B and h. Three different Reynolds numbers are taken into account. At the lowest Reynolds number considered ($Re = 200$) the spectrum is already continuous as expected for a turbulent flow. With increasing Re the spectrum extends towards higher frequencies as visible at the change-over from $Re = 200$ to 700. This trend continues for the change-over from $Re = 700$ to 10,595. Based on this observation it is clear that the low-Re cases indeed represent fully turbulent flow fields defined by a continuous spectrum. In addition to the analysis of the statistical data carried out in Sections 5.1–5.4, this finding is an additional evidence why the main flow features responsible for the dynamic behavior of the flow are found to be similar.
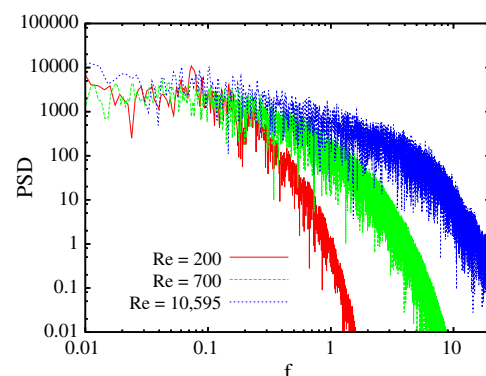

Fig. 32. Spectra of the velocity component W close to the rising slope of the second hill ($x/h = 8.3$; $y/h = 0.72$) for three different Reynolds numbers.
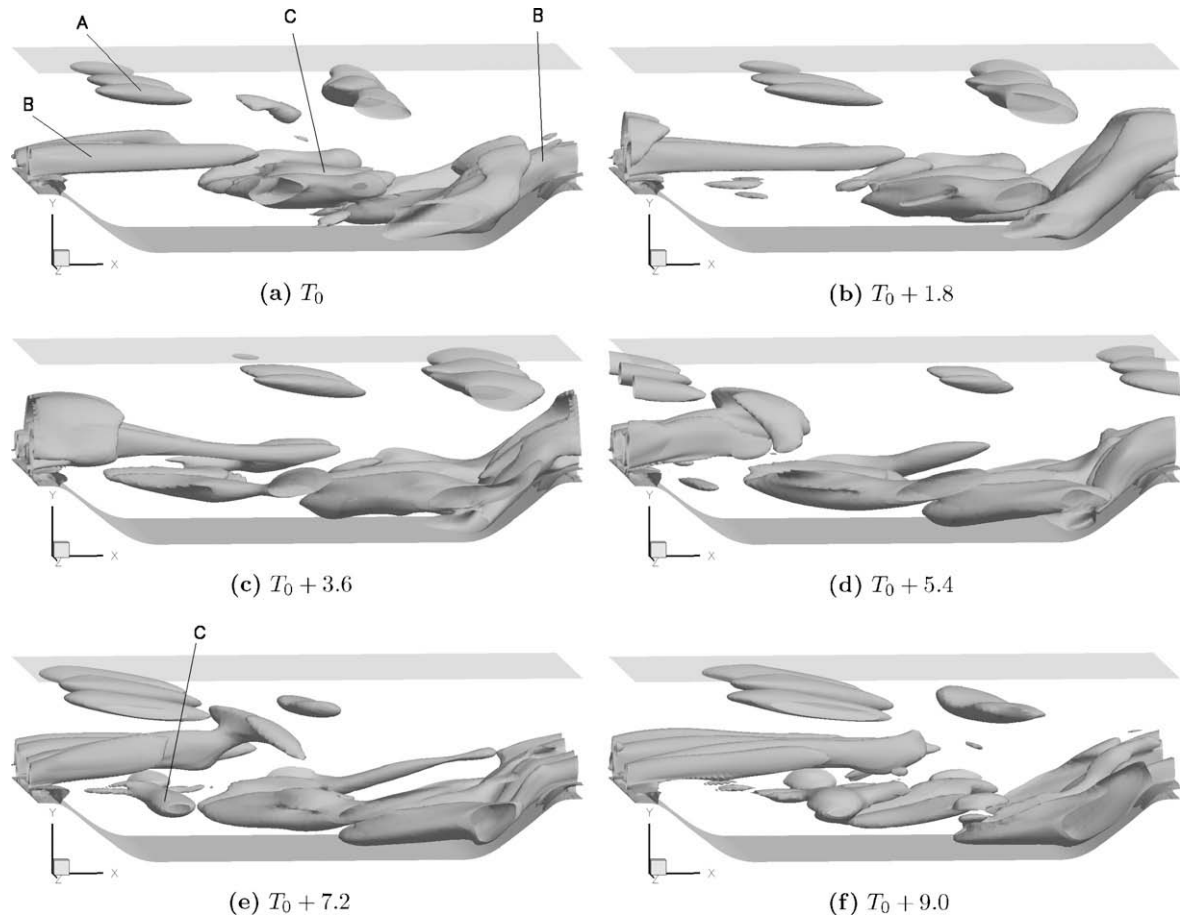
Fig. 33. Iso-surface of λ_2 (second eigenvalue of $\mathbf{S}^2 + \mathbf{\Omega}^2$, here $\lambda_2 = -0.1$); criterion used for structure identification [23]; $Re = 200$; six different phases in time representing one flow-through time.

In order to identify characteristic structures in the flow, the lowest Reynolds number at which the flow is found to be three-dimensional and instantaneous is investigated based on structure-identification methods [23]. For that purpose Fig. 33 depicts flow structures at six instants in time which represents an interval of one flow-through time. Three important flow features have to be mentioned. On the one hand elongated streamwise structures (denoted **A** in Fig. 33(a)) inclined to the wall are detected in the vicinity of the upper plane wall. They show a strong similarity to well-known streaks and are convected downstream with the mean flow.

On the other hand a variety of structures highly elongated in the streamwise direction (denoted **B**) are found close to the concave wall in front of the second hill. They are either generated by an instability due to the effect of the centrifugal forces first described by Görtler [20] or the Craik–Leibovich type-2 instability [37]. In the literature a controversy about the question which of these mechanisms is responsible for the generation of these longitudinal vortices in sheared flows over rigid wavy walls still exists (see, e.g. [18,21] and the references cited therein) with a tendency towards the latter. In the present study these vortices are extremely long at the low-*Re* case considered. They extend over the hill crest and owing to the periodic boundary conditions applied at least until half of the succeeding constriction. Similar to the first kind of structures a convective transport takes place in streamwise direction. In an experimental investigation of a channel flow with a wavy wall [21], similar streamwise structures were found above the hill crest for both laminar and turbulent flows. Furthermore, Fröhlich et al. [18] studied this flow phenomenon in great detail based on their LES predictions of the periodic hill flow at $Re = 10,595$. Although the identification of the structures at this Re is much more difficult

than for the low-*Re* case taken into account here, the outcome also supports the present findings. As expected and demonstrated in Fig. 31, the length scales in the flow increase with decreasing Reynolds number so that the extension of the structures especially in streamwise direction are substantially smaller in [18] than for the case depicted in Fig. 33.

Finally, structures denoted **C** developing in the region of the free shear layer (see region of strong vorticity in Fig. 31(b)) have to be mentioned. They are visible for instance in Fig. 33(e) and are originally aligned and elongated in spanwise direction. Here, the well-known Kelvin–Helmholtz instability is responsible for their generation. With increasing Reynolds number these structures become more and more obvious (see, e.g., vorticity plots in Fig. 31(d)–(f) for $Re = 400$, 500, and 600). Animations of the flow field over a longer time interval showed that these structures change their orientation towards the streamwise direction when convected downstream. This phenomenon is perceptible in Fig. 33(a) which depicts similar structures at a later state, again denoted **C**. At this stage oblique structures have already developed which are mainly elongated in streamwise direction but are still inclined in spanwise direction.

6. Conclusions

The paper presents a complementary numerical/experimental investigation[2] on the turbulent flow over a periodic arrangement

of hills [33] at varying Reynolds numbers in the range $100 \leqslant Re \leqslant 10,595$. A large number of different simulations using DNS and LES on very fine grids were carried out applying two fully independent numerical methods. Cross-comparison was done in three steps. In a first step the results of both codes are compared against each other. Then the predicted data are checked by cross-comparison with data from the literature [18]. Based on both steps the quality of the present predictions was carefully proven. Besides this purely numerical assessment in a third step PIV measurements were performed in a water channel involving 10 hills in streamwise direction and a large aspect ratio. These experimental data place further confidence on the results presented here.

The results achieved by this complementary study do not only support prior findings [18] at $Re = 10,595$. Furthermore, the series of predictions for the broad range of Reynolds numbers considered shed new light on the flow. In particular, the existence of a small recirculation at the foot of the windward face of the hill was confirmed for $Re = 10,595$ but also exists for $200 < Re < 10,595$. Besides, a tiny recirculation on the hill crest which has not been discussed before was found which solely exists at the highest Re. This was possible due to a new LES prediction with increased resolution supported by a series of DNS at lower Reynolds numbers. These data also allowed to investigate the behavior of the separation and reattachment length as a function of the Reynolds number. The separation length past the hill crest was found to continuously decrease with increasing Re until it reaches at minimum at $Re = 5600$ and slightly increases again for $Re = 10,595$. Even more exciting is the non-monotonous behavior of the reattachment length, which with one exception also decreases with increasing Re but shows a local minimum at $Re = 1400$. Interestingly, a small counter-rotating flow structure with positive averaged wall shear stress was detected within the main recirculation region at the falling edge of the hill between $x/h \approx 0.6$ and 0.8. This phenomenon is exclusively visible at this Reynolds number and provides an explanation for the variations of the reattachment length.

Based on the analysis of the Reynolds stresses and the behavior of the flow in the anisotropy-invariant map, it is obvious that the development of the shear layer past the hill crest is delayed and thus shifted downstream at $Re = 700$ compared to $Re = 10,595$. If this downstream shift is taken into consideration, similar states of turbulence can be found at both limiting Reynolds numbers with more distinctive extrema observed for the high-Re case. The similarity is especially pronounced for the 'splatting' phenomenon of large-scale eddies originating from the shear layer and convected downstream towards the windward slope as described in [18]. In this flow region the spanwise velocity fluctuations $\langle w'w' \rangle / U_B^2$ show nearly the same peak values and distribution for all Re studied. Nevertheless, in the remaining domain clear trends in the distributions of the mean velocities, Reynolds stresses, anisotropies and the wall shear stresses were found. As mentioned above that led for example to the observation of the tiny recirculation bubble at the hill crest at $Re = 10,595$.

Furthermore, the length scales appearing in the turbulent flow field at varying Re and the dynamic behavior of the flow were investigated taking even smaller Reynolds number into account. At $Re = 100$ the flow is found to be steady and two-dimensional. The situation changes completely at $Re \geqslant 200$ for which a three-dimensional instantaneous and chaotic flow field is observed. The corresponding spectrum at this and any higher Reynolds number considered comprises a fully continuous spectrum which extends towards higher frequencies with increasing Re. Three main flow structures can be detected already in the lowest-Re case. These are streaky structures close to the upper wall, streamwise vortices close to the concave wall in front of the second hill, and vortical structures induced by the Kelvin–Helmholtz instability of the free shear layer.

References

[1] Almeida GP, Durao DFG, Heitor MV. Wake flows behind two-dimensional model hills. Exp Thermal Fluid Sci 1993;7:87–101.
[2] Almeida GP, Durao DFG, Heitor MV. ERCOFTACdatabase, classic collection, test case C18. 2D Model Hill Wake Flows. <http://cfd.me.umist.ac.uk>; 1993.
[3] Armaly BF, Durst F, Pereira JCF, Schönung B. Experimental and theoretical investigation of backward-facing step flow. J Fluid Mech 1983;127:473–96.
[4] Benocci C, Pinelli A. The role of the forcing term in the large-eddy simulation of equilibrium channel flow. In: Rodi W, Ganić EN, editors. Engineering turbulence modeling and experiments 1. Elsevier; 1990. p. 287–96.
[5] Breuer M, Rodi W. Large-eddy simulation of complex turbulent flows of practical interest. In: Hirschel EH, editor. Flow simulation with high-performance computers II. Notes on numerical fluid mechanics, vol. 52. Vieweg; 1996. p. 258–74.
[6] Breuer M. Large-eddy simulation of the sub-critical flow past a circular cylinder: numerical and modeling aspects. Int J Numer Methods Fluids 1998;28:1281–302.
[7] Breuer M. A challenging test case for large-eddy simulation: high Reynolds number circular cylinder flow. Int J Heat Fluid Flow 2000;21(5):648–54.
[8] Breuer M. Direkte Numerische Simulation und Large-Eddy Simulation turbulenter Strömungen auf Hochleistungsrechnern, Habilitationsschrift, Universität Erlangen-Nürnberg, Berichte aus der Strömungstechnik. Shaker; 2002, ISBN: 3-8265-9958-6.
[9] Breuer M. New reference data for the hill flow test case. <http://www.hy.bv.tum.de/DFG-CNRS/>; 2005.
[10] Breuer M, Jaffrézic B, Šarić S, Jakirlić S, Deng G, Chikhaoui O, et al. Issues in hybrid LES–RANS and coarse grid LES of separated flows. In: EUROMECH colloquium 469, large-eddy simulation of complex flows. TU Dresden, Germany; October 6–8, 2005.
[11] Breuer M, Kniazev B, Abel M. Development of wall models for LES of separated flows. In: Lamballais E, Friedrich R, Geurts BJ, Métais O, editors. Sixth international ERCOFTAC workshop on DNS and LES: DLES-6, Poitiers, France, September 12–14, 2005. ERCOFTAC Series, Direct and Large-Eddy Simulation VI, vol. 10. New York: Springer Science; 2006. p. 373–80, ISBN-10 1-4020-4909-9.
[12] Breuer M, Jaffrézic B, Peller N, Manhart M, Fröhlich J, Hinterberger Ch, et al. A comparative study of the turbulent flow over a periodic arrangement of smoothly contoured hills. In: Lamballais E, Friedrich R, Geurts BJ, Métais O, editors. Sixth international ERCOFTAC workshop on DNS and LES: DLES-6, Poitiers, France, September 12–14, 2005, ERCOFTAC Series. Direct and Large-Eddy Simulation VI, vol. 10. New York: Springer Science; 2006. p. 635–42, ISBN-10 1-4020-4909-9.
[13] Breuer M, Kniazev B, Abel M. Development of wall models for LES of separated flows using statistical evaluations. Comput Fluids 2007;36(5):817–37.
[14] Breuer M, Jaffrézic B, Arora K. Hybrid LES–RANS technique based on a one-equation near-wall model. J Theor Comput Fluid Dyn 2008;22(3–4):157–87.
[15] Eckelmann H. Einführung in die Strömungsmesstechnik, Leitfaden der angewandten Mathematik und Mechanik, 74, Teubner; 1997 .
[16] Eggels JGM, Unger F, Weiss MH, Westerweel J, Adrian RJ, Friedrich R, et al. Fully developed turbulent pipe flow: a comparison between direct numerical simulation and experiment. J Fluid Mech 1994;268:175–209.
[17] Friedrich R, Hüttl T, Manhart M, Wagner C. Direct numerical simulation of incompressible turbulent flows. Comput Fluids 2001;30(5):555–79.
[18] Fröhlich J, Mellen CP, Rodi W, Temmerman L, Leschziner MA. Highly resolved large-eddy simulation of separated flow in a channel with streamwise periodic constrictions. J Fluid Mech 2005;526:19–66.
[19] Germano M, Piomelli U, Moin P, Cabot WH. A dynamic subgrid-scale eddy viscosity model. Phys Fluids A 1991;3(7):1760–5.
[20] Görtler H, Über eine dreidimensionale Instabilität laminarer Grenzschichten an konkaven Wänden. Nachr Ges Wiss Göttingen, Math-Phys Klassse, Neue Folge I 1940;2:1–26.
[21] Günther A, von Rohr PR. Large-scale structures in a developed flow over a wavy terrain. J Fluid Mech 2003;478:257–85.
[22] Jakirlić S, Jester-Zürker R, Tropea C. editors. 9th ERCOFTAC/IAHR/COST workshop on refined flow modeling. Germany: Darmstadt University of Technology; October 4–5, 2001.

[23] Jeong J, Hussain F. On the identification of a vortex. J Fluid Mech 1995;285:69–94.
[24] Jovanović J. Statistical dynamics of turbulence. Springer; 2004.
[25] Kim J, Moin P, Moser RD. Turbulence statistics in fully developed channel flow at low Reynolds number. J Fluid Mech 1987;177:133–66.
[26] Lilly DK. A proposed modification of the Germano subgrid-scale closure method. Phys Fluids A 1992;4(3):633–5.
[27] Lumley JL, Newman G. The return to isotropy of homogeneous turbulence. J Fluid Mech 1977;82:161–78.
[28] Lumley JL. Computational modeling of turbulent flows. Adv Appl Mech 1978;18:123–76.
[29] Manceau R, Bonnet JP, Leschziner MA, Menter F, editors. 10th Joint ERCOFTAC(SIG-15)/IAHR/QNET-CFD workshop on refined flow modeling. France: Université de Poitiers; October 10–11, 2002.
[30] Manhart M, Friedrich R. DNS of a turbulent boundary layer with separation. Int J Heat Fluid Flow 2002;23(5):572–81.
[31] Manhart M. A zonal grid algorithm for DNS of turbulent boundary layers. Comput Fluids 2004;33(3):435–61.
[32] Manhart M, Peller N, Brun C. Near-wall scaling for turbulent boundary layers with adverse pressure gradient. J Theor Comput Fluid Dyn 2008;22(3–4):243–60.
[33] Mellen CP, Fröhlich J, Rodi W. Large-eddy simulation of the flow over periodic hills, In: Deville M, Owens R, editors. Proceedings of 16th IMACS world congress, Lausanne, Switzerland. CD-ROM; 2000.
[34] Moser RD, Kim J, Mansour NN. Direct numerical simulation of turbulent channel flow up to $Re_\tau = 590$. Phys Fluids A 1999;11(4):943–5.
[35] Peller N, Le Duc A, Tremblay F, Manhart M. High-order stable interpolations for immersed boundary methods. Int J Numer Methods Fluids 2006;52:1175–93.
[36] Peller N, Manhart M. Turbulent channel flow with periodic hill constrictions. Notes on numerical fluid mechanics and multidisciplinary design 92. New results in numerical and experimental fluid mechanics. Edition V. New York: Springer; 2006. p. 504–12, ISBN 3-540-33286-3.
[37] Phillips WRC, Wu Z. On the instability of wave-catalyzed longitudinal vortices in strong shear. J Fluid Mech 1994;272:235–54.
[38] Piomelli U, Chasnov JR. Large-eddy simulations: theory and applications. In: Hallbäck M, Henningson DS, Johansson AV, Alfredson PH, editors. Turbulence and transition modeling. Kluwer; 1996. p. 269–331.
[39] Pope SB. Turbulent flows. Cambridge University Press; 2000.
[40] Rapp Ch, Manhart M. Experimental investigations on the turbulent flow over a periodic hill geometry. In: Fifth international symposium on turbulence and shear flow phenomena, August 27–29, 2007, Garching, Germany.
[41] Rhie CM, Chow WL. A numerical study of the turbulent flow past an isolated airfoil with trailing edge separation. AIAA J 1983;21:1525–32.
[42] Rodi W, Bonnin CJ, Buchal T, editors. In: Proceedings of the ERCOFTAC workshop on data bases and testing of calculation methods for turbulent flows. In association with 4th ERCOFTAC/IAHR workshop on refined flow modeling. Germany: University of Karlsruhe; April 3–7, 1995.
[43] Šarić S, Jakirlić S, Breuer M, Jaffrézic B, Deng G, Chikhaoui O et al. Evaluation of detached-eddy simulations for predicting the flow over periodic hills. In: Eric Cancès and Jean-Frédéric Gerbeau, editors. ESAIM Proceedings CEMRACS 2005 (Centre d'été Mathématique de Recherche Avancée en Calcul Scientifique). Computational aeroacoustics and computational fluid dynamics in turbulent flows, Marseille, France, July 18–August 26, 2005. vol. 16, 2007. p. 133–45.
[44] Schumann U. Subgrid-scale model for finite-difference simulations of turbulent flows in plane channels and annuli. J Comput Phys 1975;18:376–404.
[45] Smagorinsky J. General circulation experiments with the primitive equations, I, the basic experiment. Mon Weather Rev 1963;91:99–165.
[46] Stone HL. Iterative solution of implicit approximations of multidimensional partial differential equations. SIAM J Numer Anal 1968;5:530–58.
[47] Temmerman L, Leschziner MA. Large-eddy simulation of separated flow in a streamwise periodic channel constriction. In: Lindborg A, Johansson E, Eaton J, Humphrey J, Kasagi N, Leschziner M, Sommerfeld M, editors. Second international symposium turbulence and shear flow phenomena, Stockholm, June 27–29, 2001. p. 399–404.
[48] Temmerman L, Leschziner MA, Mellen CP, Fröhlich J. Investigation of wall-function approximations and subgrid-scale models in large-eddy simulation of separated flow in a channel with periodic constrictions. Int J Heat Fluid Flow 2003;24:157–80.
[49] Werner H, Wengle H. Large-eddy simulation of turbulent flow over and around a cube in a plate channel. In: F.Durst et al., editors. 8th Symposium on turbulent shear flows. Springer; 1993.